Schweizerischer Erdbebendienst
Service Sismologique Suisse
Servizio Sismico Svizzero
Swiss Seismological Service

ETH zürich

SITE CHARACTERIZATION REPORT

SARD: Ardez (GR) - Schule

Manuel Hobiger, Francesco Panzera, Donat Fäh

Last Modification: 09/11/2020

Schweizerischer Erdbebendienst (SED)
Service Sismologique Suisse
Servizio Sismico Svizzero
Servizi da Terratrembels Svizzer

ETH Zürich
Sonneggstrasse 5
8092 Zürich
Schweiz
manuel.hobiger@sed.ethz.ch

Contents

Summary

The free-field strong-motion station SARD was built in Ardez (GR) close to the school. We performed a passive seismic array measurement with two array configurations to characterize the soil underneath the station.
The measurements show that the fundamental frequency of the structure beneath the station is about 8 Hz. We cannot retrieve dispersion curves for both array configurations, but only for subarrays of the smaller array. The array measurements were analyzed with different techniques, namely 3-component HRFK, WaveDec and SPAC. All techniques gave similar dispersion curves. The dispersion curves for Love and Rayleigh waves are retrieved between 7.9 to 30 Hz for Love waves and from 8.6 to 44.1 Hz for Rayleigh waves.
The best velocity profiles were obtained by a joint inversion of Love and Rayleigh wave dispersion curves with or without ellipticity information, where the Rayleigh wave ellipticity angle was corresponding to a retrograde particle motion in the whole frequency range. The structure can be explained by models with a main impedance contrast at 8 m depth for inversions without ellipticity target, or by a more gradual increase of the shear-wave velocity for inversions including the ellipticity curve. The V_{S30} of the best models for the first inversion target is about 547 m/s, corresponding to soil class E in both EC8 and SIA261. For the other inversion target, V_{S30} is about 470 m/s, corresponding to soil class B in EC8 and E in SIA261. For the ensemble of both targets, V_{S30} is about 509 m/s and the site belongs to class E in SIA261 and is on the border between B and E in EC8.

1 Introduction

In the framework of the second phase of the Swiss Strong Motion Network (SSMNet) renewal project, a new station was planned in the Lower Engadine. The school of Ardez (GR) was selected as installation site. The new station, called SARD, went operational on 15 July 2015. The location of the station is shown in Fig. 1.

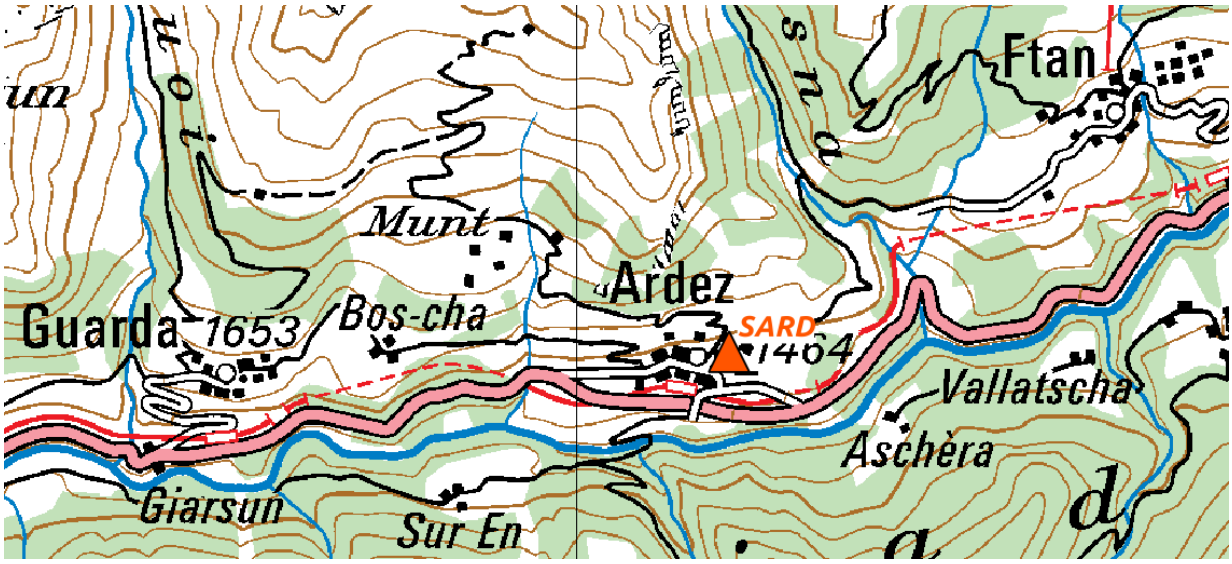

Figure 1: Map showing the location of station SARD.

2 Geological setting

A geological map of the surroundings of station SARD is shown in Fig. 2. The school is located on dolomite outcropping the surrounding moraine, station SARD is located on the transition zone between both. Most stations of the passive seismic array were located on either moraine or dolomite, but at least one was located on alluvial deposits.

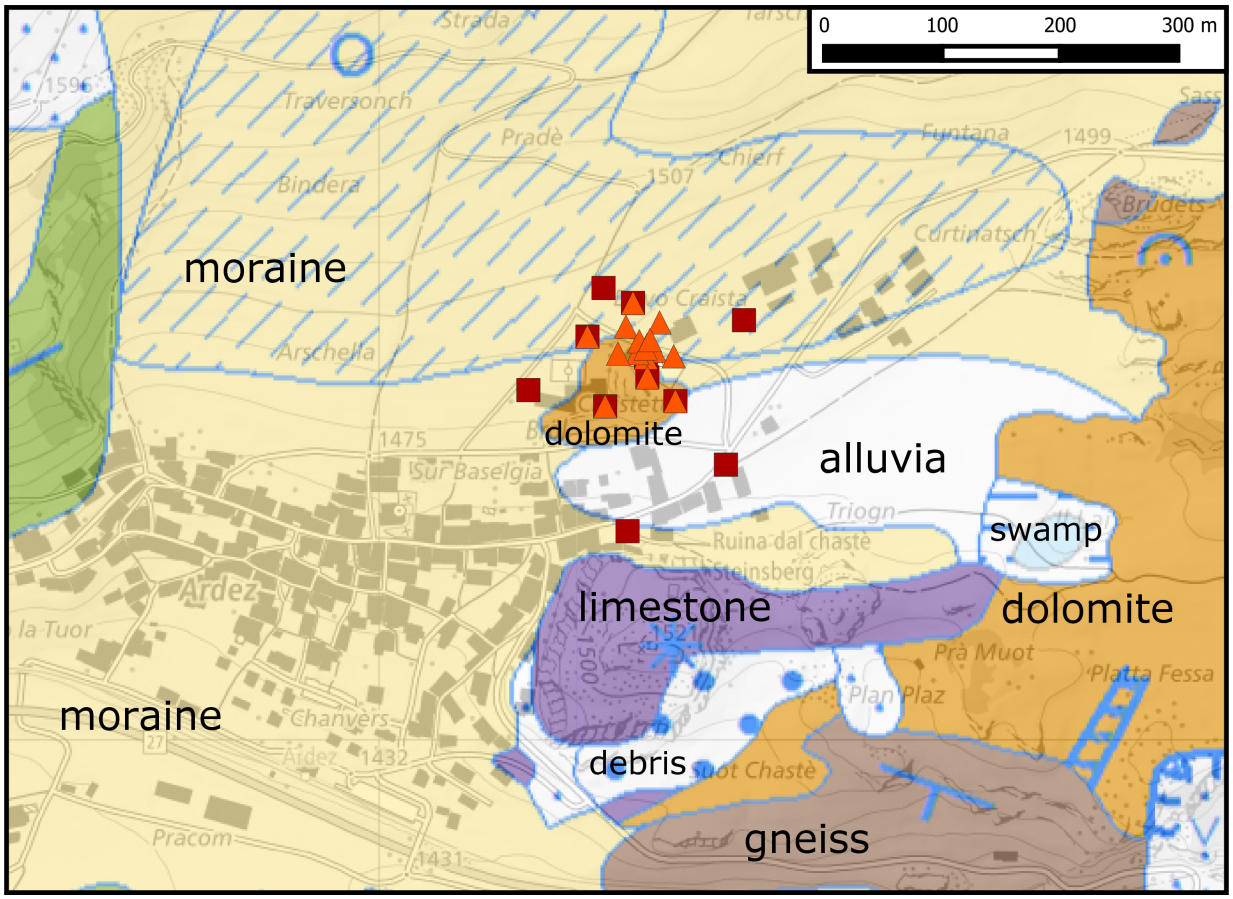

Figure 2: Geological map of the area around station SARD, highlighting the location of the array stations (see next section). According to the geological atlas, station SARD lies on the transition zone between dolomite outcrop and moraine. ©2020 swisstopo (JD100042)

3 Site characterization measurements

3.1 Data set

In order to characterize the local underground structure around station SARD, passive seismic array measurements were carried out on 11 October 2015. The layout of the seismic measurements is shown in Fig. 3.
Two array measurements were performed (see Table 1 for the main characteristics). The first array was planned to consist of 16 stations, but one was not running (the gray station in Fig. 3). This array was planned to consist of three rings of five stations each and a central station, with ring radii of 8 m, 25 m and 50 m, respectively. The center of the outermost ring was shifted towards southwest with respect to the inner rings.
The second array consisted of the outermost ring of the first array and an additional ring with radius of around 100 m, whose center was shifted southwards from the first array. Two stations of the inner rings of the first array were kept as central stations for this array.
As will be shown later, the array processing of arrays 1 and 2 did not yield useful dispersion curves. Therefore, two subarrays were formed out of the first array. The first subarray, called array 3, consists of the two innermost rings and the central station of array 1. The second subarray, named array 4, includes only the central ring and the central station.
The names of the stations of the first array (and therefore also subarrays 3 and 4) are composed of "SARD" followed by a two-digit number (01 to 03, 05 to 12, 22, 26, 28, 30). The seismic stations consisted of Lennartz 3C 5 s sensors connected to Quanterra Q330 digitizers. A total of 12 digitizers were used, but one was not recording. Eleven working sensors were connected to the A channels of the digitizers and four sensors to B channels. The station names in the second array are composed of "SARD" and a two-digit number between 51 and 76 (51, 52, 53, 55, 56, 57, 58, 59, 61, 62, 76).
The station locations have been measured by a differential GPS system (Leica Viva GS10) which was set up to measure with a precision better than 5 cm. This precision was achieved for all stations.
In the inner parts of the array, an additional experiment was carried out, generating seismic waves with a sledgehammer at five shot points, generating 10 shots per point.

Table 1: List of the passive seismic array measurements in Ardez. Arrays 3 and 4 are sub-arrays of array 1.

Array name	Number of sensors	Minimum interstation distance [m]	Maximum interstation distance [m]	Recording time [s]
1	15	7.8	92.5	5580
2	11	16.8	207.1	7320
3	11	7.8	47.7	5580
4	6	7.8	15.3	5580

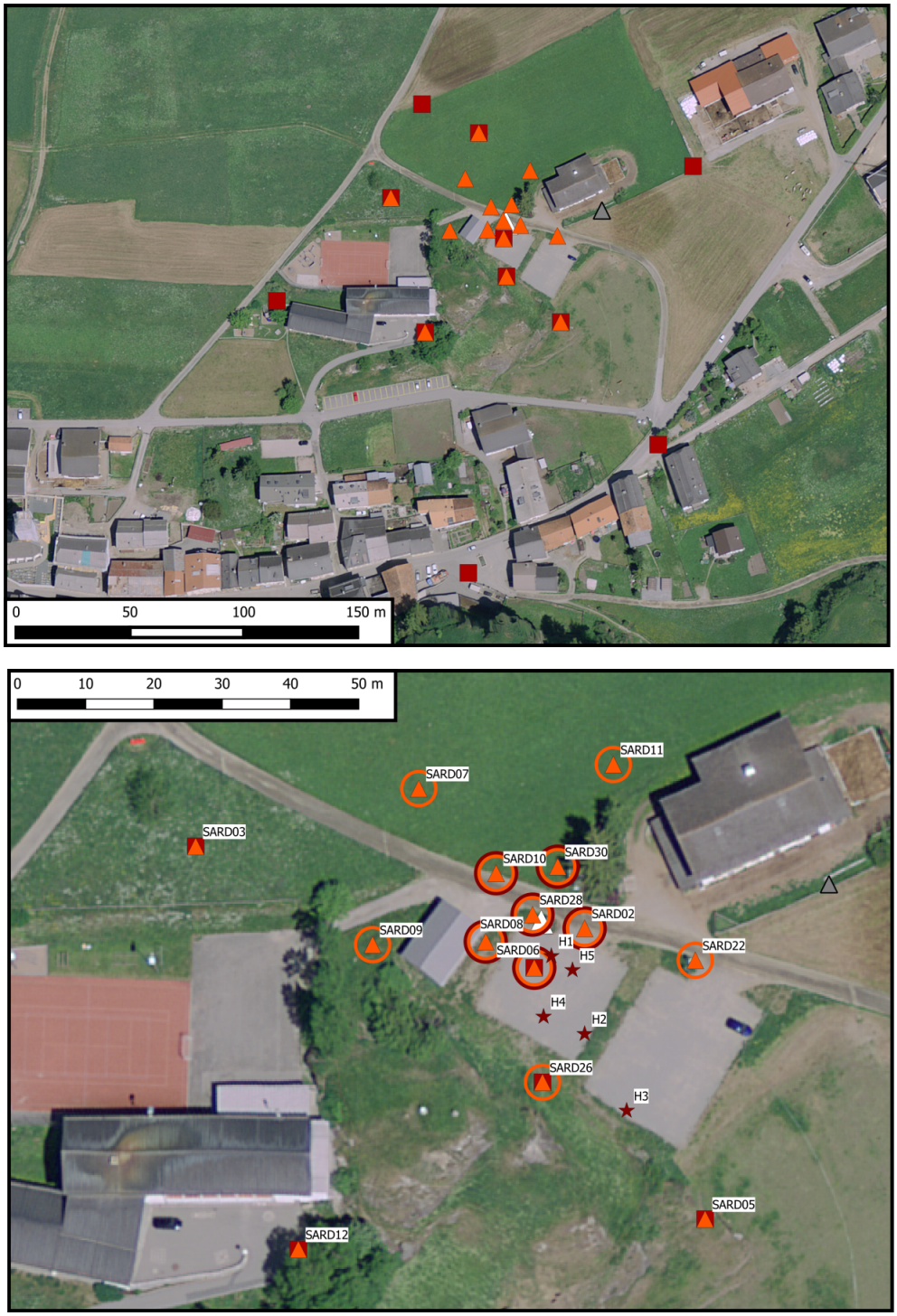

Figure 3: Top: Layout of the array measurements around station SARD. The location of SARD is indicated by the white triangle, the locations of the stations for the passive seismic measurement by the orange triangles (first array) and red squares (second array). The gray triangle shows the locations of the sensor which was not recording. Bottom: Zoom on the central part of the arrays. The stations of subarray 3 and 4 are represented by the orange and red circles, respectively, around the stations. The hammer shot locations of the additional sledgehammering experiment are indicated by the red stars. ©2020 swisstopo (JD100042)

3.2 H/V and RayDec ellipticity curves

Figure 4 shows the H/V curves determined with the time-frequency analysis method (Fäh et al., 2009) for all stations of both passive arrays. The curves show a wide variability for all stations. Some stations show peaks between 0.7 and 1.0 Hz, others around 1.5 Hz. Most stations have clear peaks between 4 and 17 Hz, which we interpret as the fundamental frequency of the site.
The RayDec technique (Hobiger et al., 2009) is supposed to eliminate the contributions of other wave types than Rayleigh waves and give a better estimate of the ellipticity than the classical H/V technique. The RayDec ellipticity curves for all stations of the array measurements are shown in Fig. 4 and are similar to the H/V curves. At lower frequencies, there are no very pronounced peaks and the amplitudes are very variable. A common feature for the stations of array 4, the innermost part of array 1, is a clear ellipticity peak at around 8 Hz. For the other stations of array 2, this feature is still visible, but the frequencies vary.

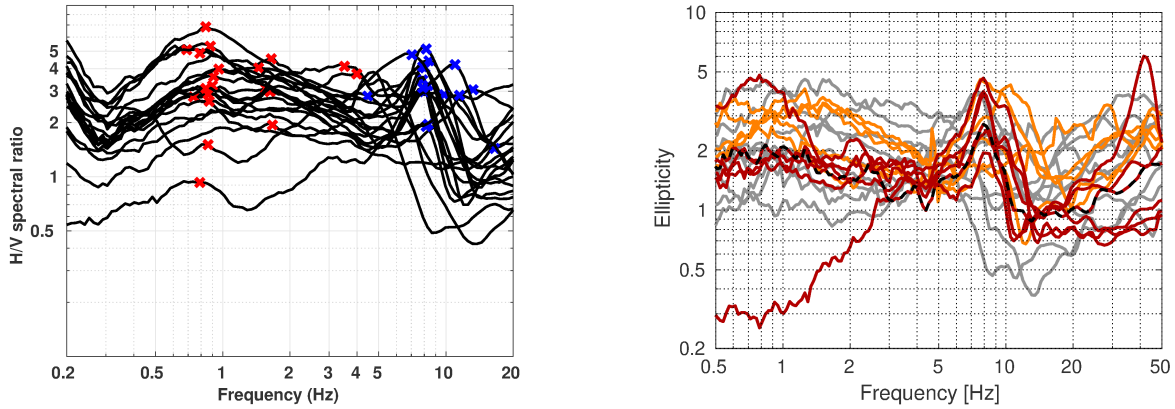

Figure 4: Left: Overview of the H/V measurements for the different stations of both array measurements. Right: RayDec ellipticities for all measurement stations. The orange curves belong to stations of array 3, the red curves to stations of array 4. The red-black dashed curve belongs to station SARD28, the the station located closest to the permanent station SARD.

3.3 Polarization analysis

The polarization analysis was performed according to Burjánek et al. (2010) and Burjánek et al. (2012). The results for all stations reflect the variability of the underground in the area. Only the results for SARD28, the station closest to SARD, are shown here.
Around 8 Hz, the ellipticity peak frequency, some hints of a polarized particle motion are visible, but not strong enough to interpret them as 2-dimensional polarization effects. In any case, the predominant strike direction at this frequency is along the direction of the slope.

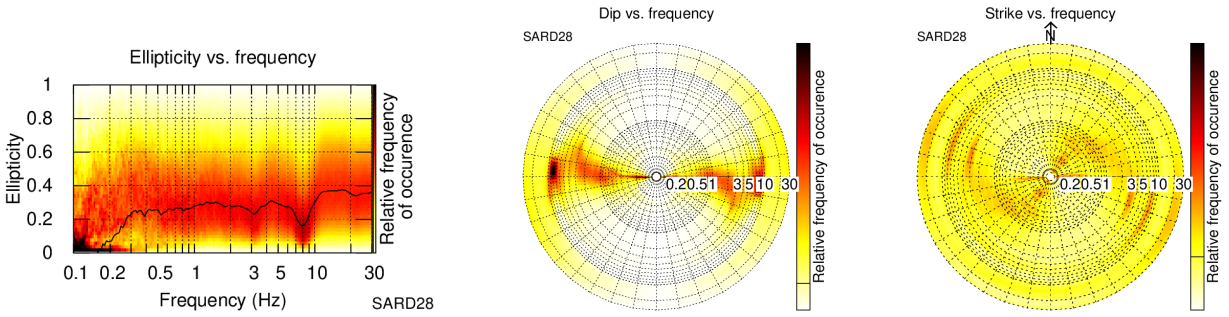

Figure 5: Polarization analysis of station SARD28.

3.4 3-component high-resolution FK

The results of the 3-component high-resolution FK analysis (Poggi and Fäh, 2010) for arrays 1 and 2 are shown in Fig. 6. On all three components, no dispersion curves can be identified.
Therefore, the data of array 1 were reanalyzed using only the innermost stations (arrays 3 and 4). The results of this processing are shown in Fig. 7. As array 4 has a smaller aperture, it also has a smaller resolution range than array 3.
On the transverse component, corresponding to Love waves, we can clearly identify a dispersion curve for array 3 from 7.9 up to 28.5 Hz and for array 4 from 10.3 to 29.6 Hz, covering the entire accessible frequency range for each array.
On the vertical component, corresponding to Rayleigh waves, we can clearly identify one mode between 11.8 and 28.9 Hz for array 3 and between 12.9 and 26.5 Hz for array 4, where array 3 does not reach the theoretical lower resolution limit of the array. On the radial component, also related with Rayleigh waves, we can identify a dispersion curve between 8.6 and 29.0 Hz for array 3 and between 12.1 and 14.0 Hz for array 4.
The corresponding ellipticity curves of these modes (Fig. 8) do not show pronounced peaks and will be compared with the single-station ellipticity curves at a later stage.

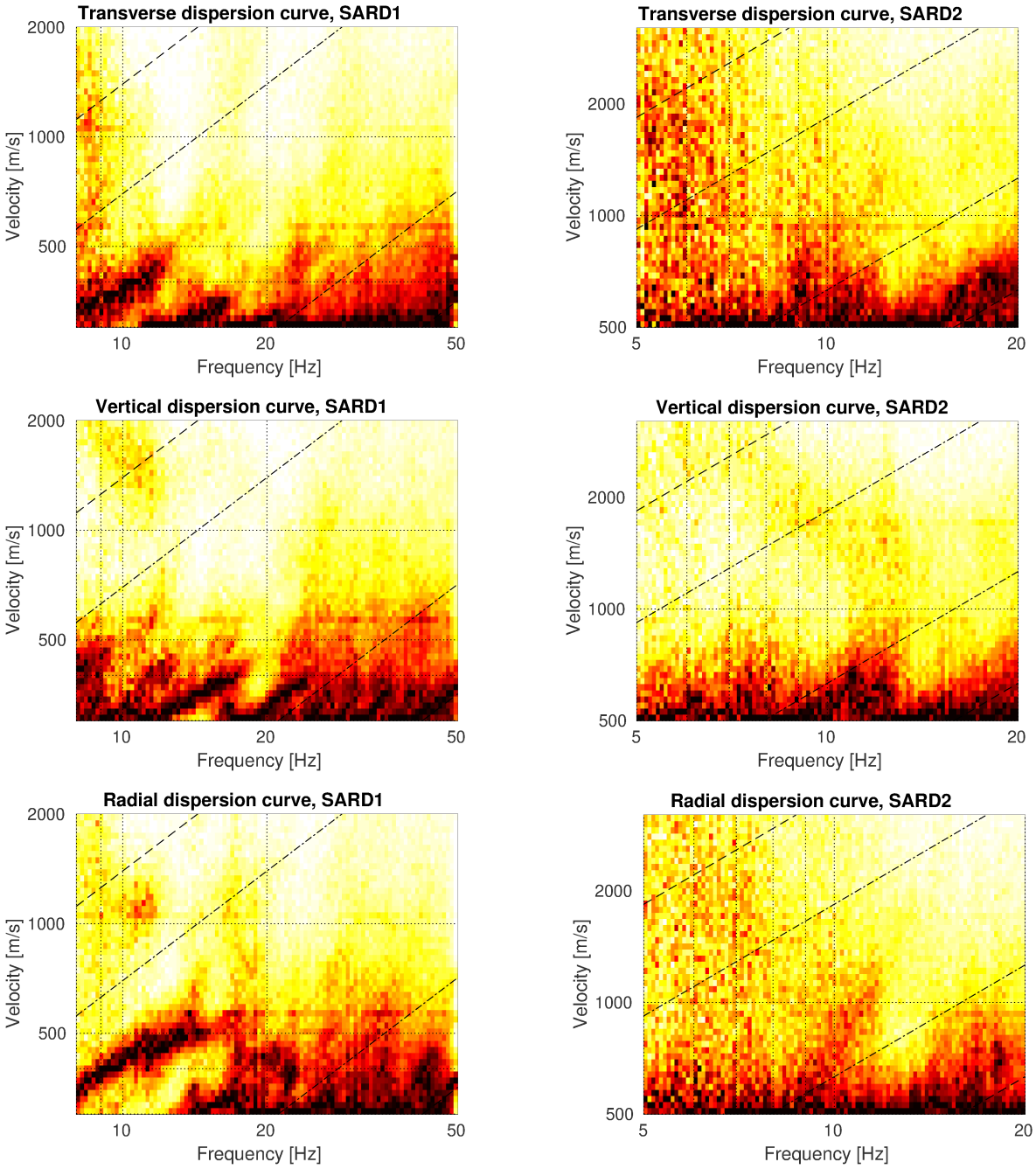

Figure 6: Dispersion curves obtained with the 3-component HRFK algorithm (Poggi and Fäh, 2010). From top to bottom, the dispersion curves for the transverse, vertical and radial components are shown for array 1 (left column) and array 2 (right column). The dashed and dotted black lines are the array resolution limits.

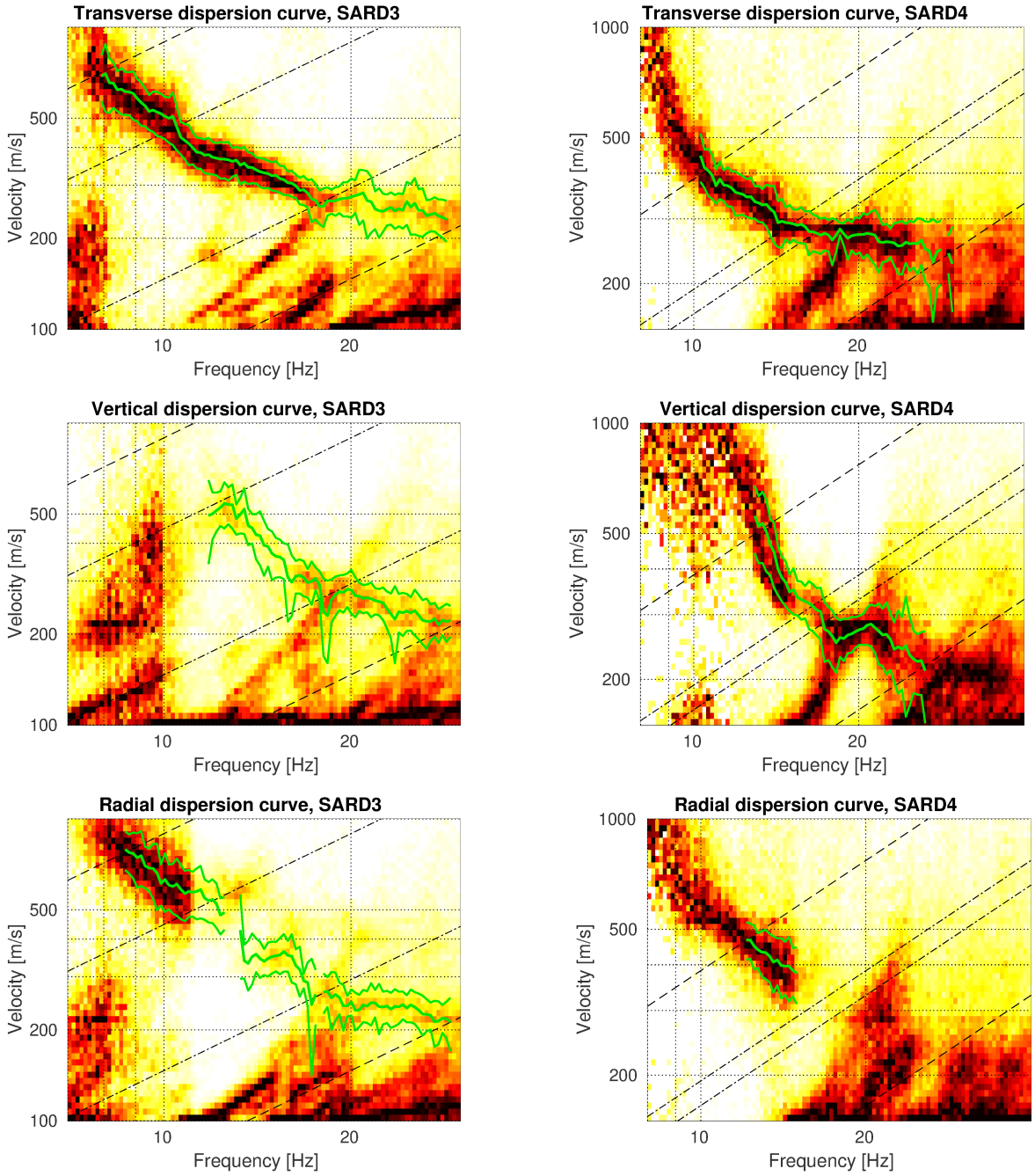

Figure 7: Dispersion curves obtained with the 3-component HRFK algorithm (Poggi and Fäh, 2010). From top to bottom, the dispersion curves for the transverse, vertical and radial components are shown for array 3 (left column) and array 4 (right column). The dashed and dotted black lines are the array resolution limits. The solid green lines are picked from the data, where the central line indicates the best values and the two outer lines the standard deviation.

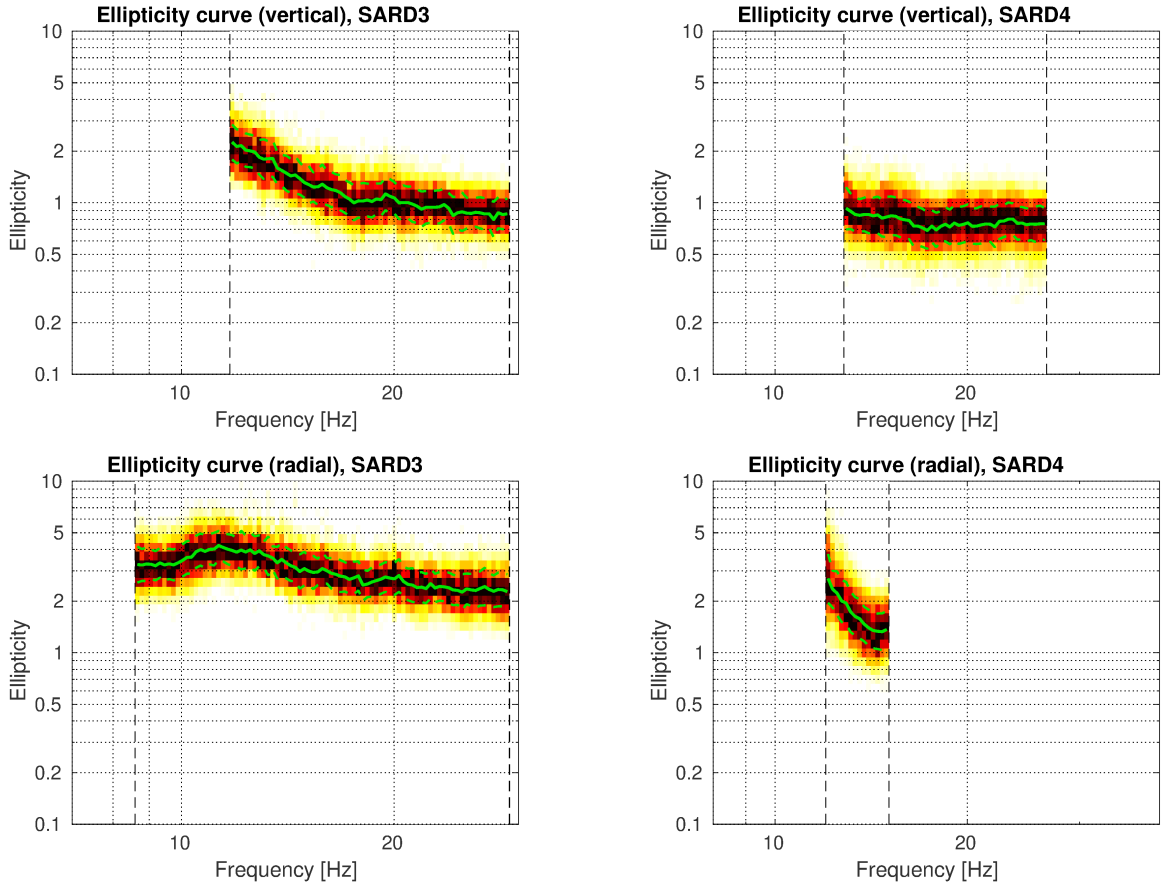

Figure 8: Ellipticity curves obtained with the 3-component HRFK algorithm (Poggi and Fäh, 2010) corresponding to the picked dispersion curves on the vertical and radial components for array 3 (left column) and array 4 (right column). The solid green lines are picked from the data, where the central line indicates the best values and the two outer lines the standard deviation.

3.5 WaveDec

The results of the WaveDec (Maranò et al., 2012) processing are shown in Figs 9 and 10. This technique estimates the properties of single or multiple waves simultaneously with a maximum likelihood approach. In order to improve the results, the parameter γ, which modifies the sharpness of the wave property estimation, has been tuned. Here, a value of $\gamma = 0.2$ was used, corresponding to a predominantly maximum likelihood estimation. The processing for arrays 1 and 2 did not yield meaningful results. Only the results for arrays 3 and 4 are shown.

The Love wave dispersion curve for array 3 is well retrieved between 8.7 and 25.5 Hz. For array 4, the curve is picked between 10.2 and 28.4 Hz.

For Rayleigh waves, the results are less clear, but a dispersion curve can be picked between 8.7 and 25.5 Hz for array 3 and between 11.3 and 20.4 Hz for array 4. The ellipticity angles for the picked Rayleigh wave dispersion curves are negative for both arrays, corresponding to retrograde particle motion. For array 3, however, there is an ambiguity around 10 Hz, as the angle is close to -90° there and might as well be prograde.

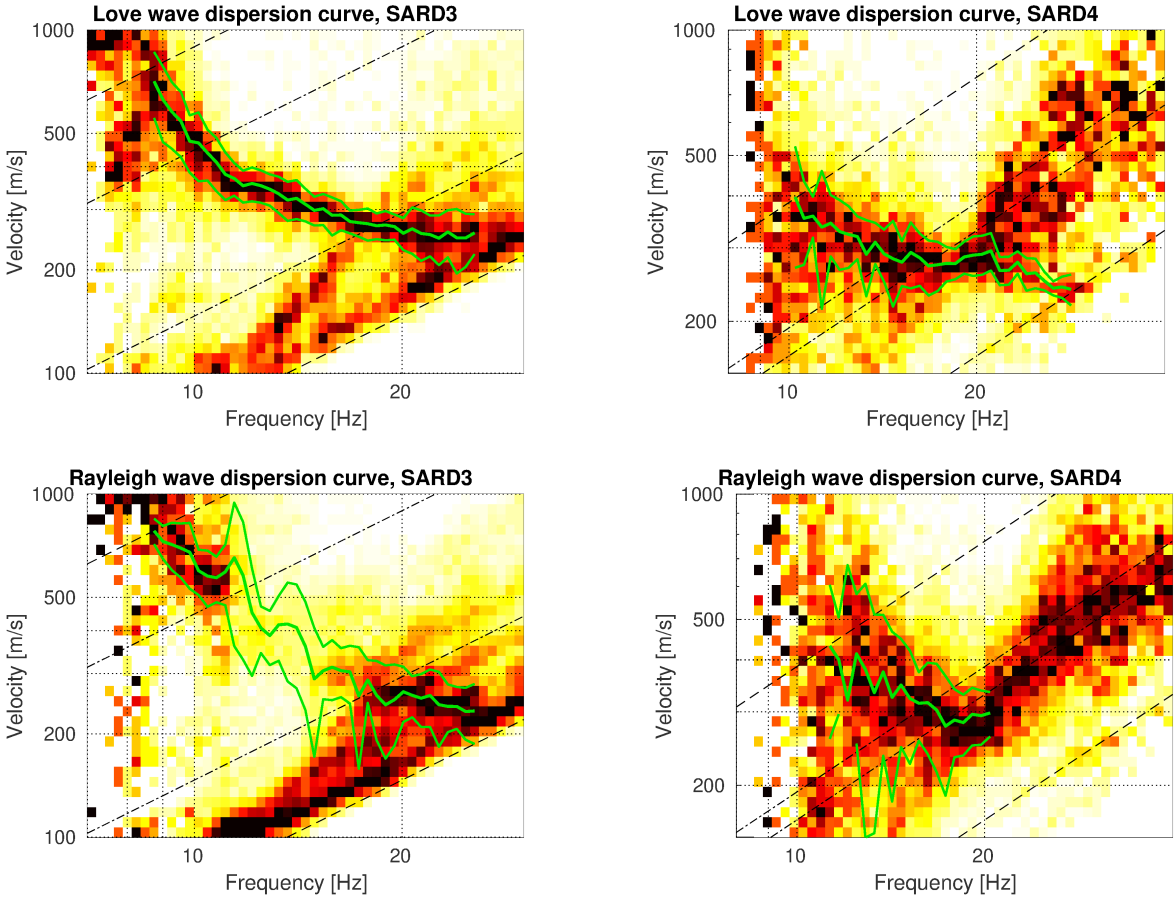

Figure 9: Love (top line) and Rayleigh (bottom line) wave dispersion curves obtained with the WaveDec technique (Maranò et al., 2012) for array 3 (left) and array 4 (right). The dashed lines indicate the theoretical array resolution limits.

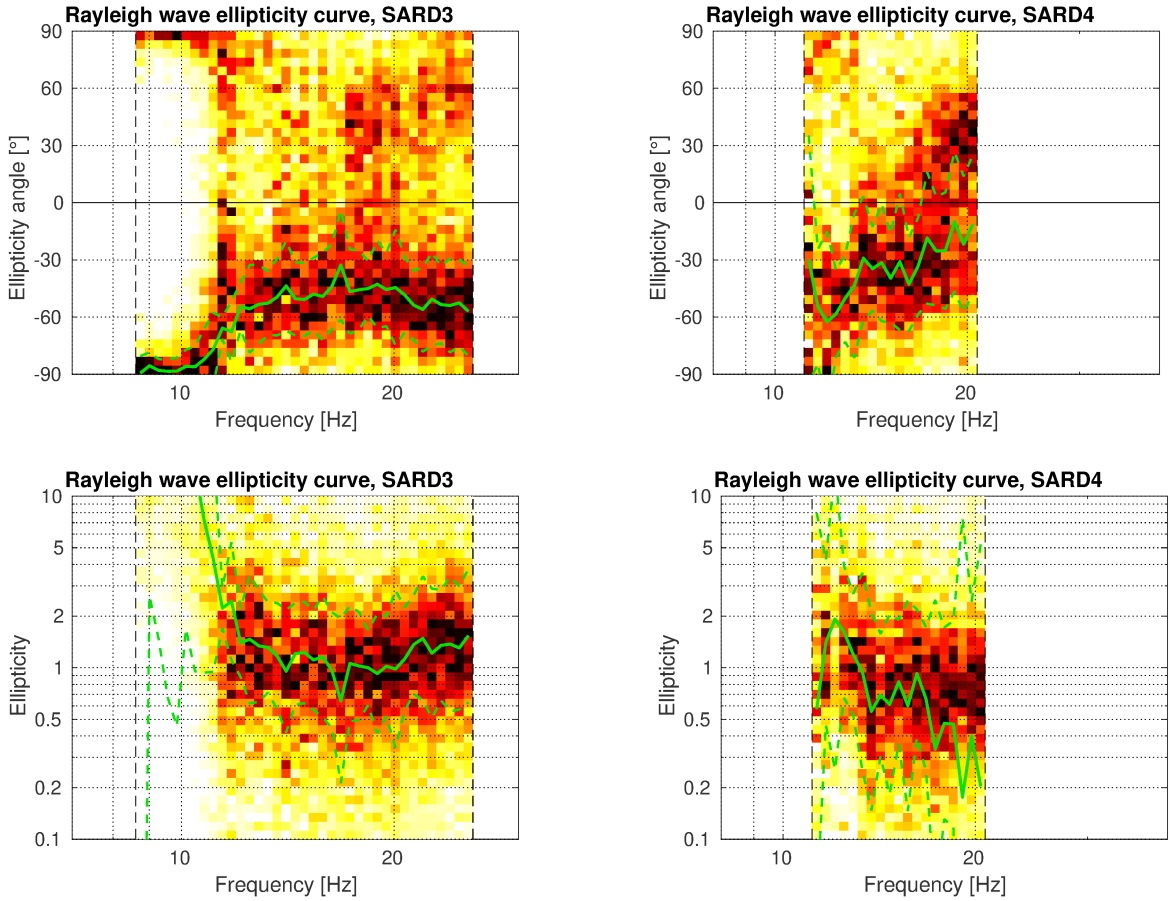

Figure 10: Rayleigh wave ellipticity curves obtained with the WaveDec technique (Maranò et al., 2012). Top line: Rayleigh wave ellipticity angles obtained using array 3 (left) and array 4 (right). Bottom line: Rayleigh wave ellipticity curve, i.e. the absolute value of the tangent of the ellipticity angle, for the curve of array 3 (left) and array 4 (right).

3.6 SPAC

The SPAC (Aki, 1957) curves of the vertical components have been calculated using the M-SPAC (Bettig et al., 2001) technique implemented in geopsy. Rings with different radius ranges had been defined previously and for all station pairs with distance inside this radius range, the cross-correlation was calculated over a wide frequency range. These cross-correlation curves are averaged for all station pairs of the respective ring and give the SPAC curves. The rings are defined in such a way that at least three station pairs contribute and that their connecting vectors have a good directional coverage.
For array 2, the retrieved SPAC curves have no similarity with the theoretical Bessel functions. The same is the case for the large-distance station pairs of array 1. Therefore, only the data of the inner station pairs, i.e. array 3, were used, limiting the inter-station distances to less than 18 m. The SPAC curves for the four defined rings are shown in Fig. 11. The black points indicate the data values which contributed to the final dispersion curve estimation, which was made with the function `spac2disp` of the geopsy package. The resulting dispersion curve is shown in Fig. 11 as well.
The SPAC curves have the shape of the theoretical Bessel functions. The retrieved Rayleigh wave dispersion curve ranges from 10.2 to 18.8 Hz.

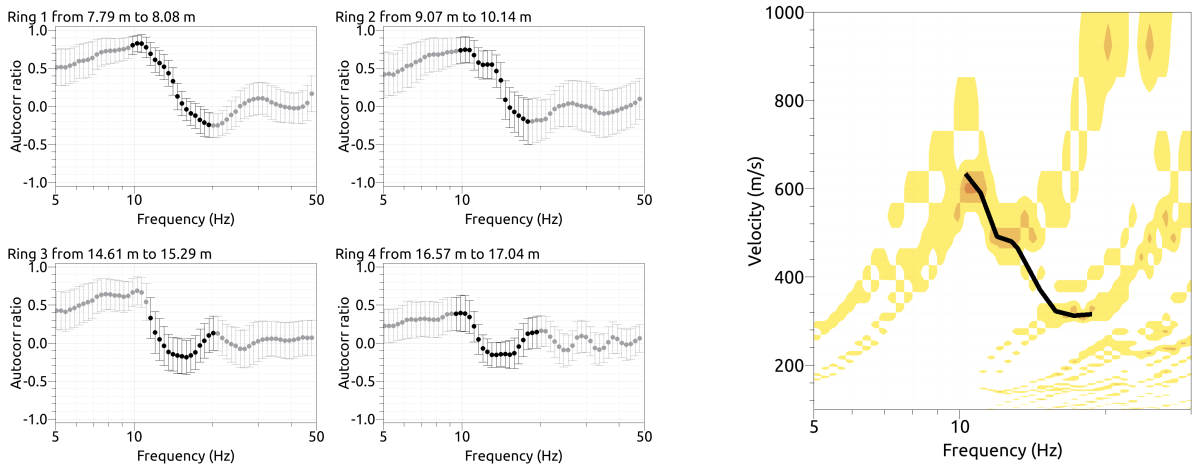

Figure 11: Left: SPAC curves for four rings of array 3. The black data points contributed to the dispersion curve estimation. Right: resulting Rayleigh wave velocities. The black line corresponds to the picked dispersion curve.

3.7 WaveDecActive

An additional active measurement was performed. At five shot points, seismic signals were generated by hammering with a sledgehammer. See Fig. 3 for the locations of the hammer shots. Stations of array 1 were used to analyze the data. As close stations tend to clip in such an experiment, such data were removed for the analysis. Distant stations, where the hammering signal is not distinguishable from the noise level, were also removed. For each shot point, different stations contribute to the measurement.
The data were analyzed using the WaveDecActive code (Maranò et al., 2017), which works similar to WaveDec, but analyzes data from active shots at known shot locations. The results are shown in Fig. 12. A Rayleigh wave dispersion curve was picked between 20.5 and 44.1 Hz.
As the hammering was performed on a horizontal plate, no Love waves were generated and analyzed.

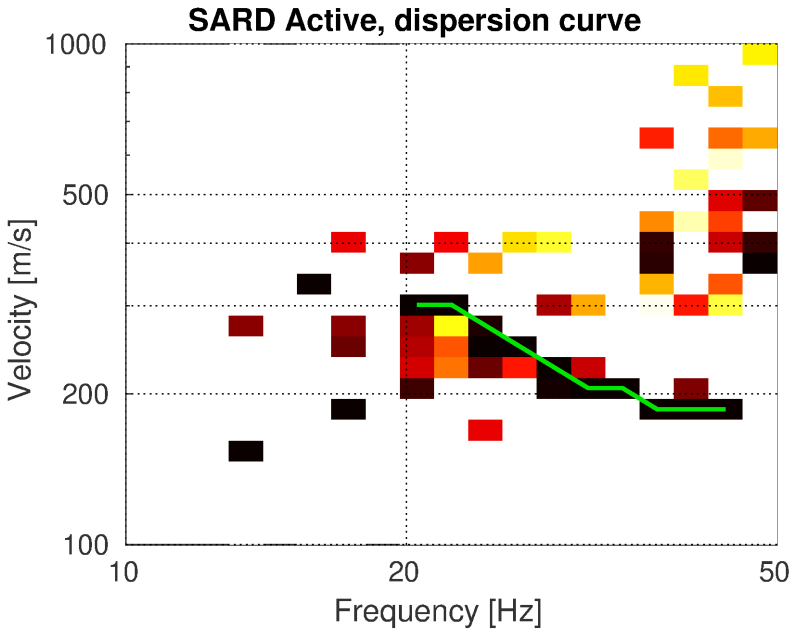

Figure 12: Rayleigh wave dispersion curve obtained with the WaveDecActive technique (Maranò et al., 2012) for array 1. The green curve was manually picked.

3.8 Summary

Fig. 13 gives an overview of the dispersion and ellipticity curves determined by the different methods.
For Love waves, the HRFK and WaveDec results for the respective arrays are in good overall agreement. For array 3, there is larger difference for both methods in the low-frequency part. We can attribute a dispersion curve for Love waves from 7.9 to almost 30 Hz.
For Rayleigh waves, there is also a good overall agreement between the different methods. The WaveDec curve for array 4 was difficult to pick at low frequencies (see Fig. 9) and shows deviations from the other methods at lower frequencies. The SPAC curve covers a smaller frequency range than the other methods, but is in very good agreement with them. The WaveDecActive dispersion curve shows higher velocities between 20 and 30 Hz, but seems to be a good continuation of the other curves above that frequency. Combining the different methods, we can attribute a dispersion curve from 8.6 to 44.1 Hz.
The ellipticity curves retrieved using the different methods agree less. The single-station ellipticity curve determined with RayDec shows a clear peak at around 8 Hz, but it is unclear if it corresponds to a singularity or not. The WaveDec curves were picked as retrograde ellipticity angles, but they might as well be prograde below 12 Hz. This might be linked with lateral variations in the surroundings. The HRFK curves are not in agreement with the other curves.
The RayDec curve was transformed to ellipticity angle by using the arctan function. As we cannot distinguish between prograde and retrograde particle motion with a single-station method, we account for both possibilities and the RayDec (and HRFK) curves are represented twice, once for each sense of rotation. The ellipticity angle representation does not help us to determine if the particle motion actually is retrograde or prograde between 8 and 12 Hz. The RayDec curve has a slight trough at around 12 Hz, so if the peak at 8 Hz would correspond to a singularity, the particle motion between 8 and 12 Hz would need to be prograde.

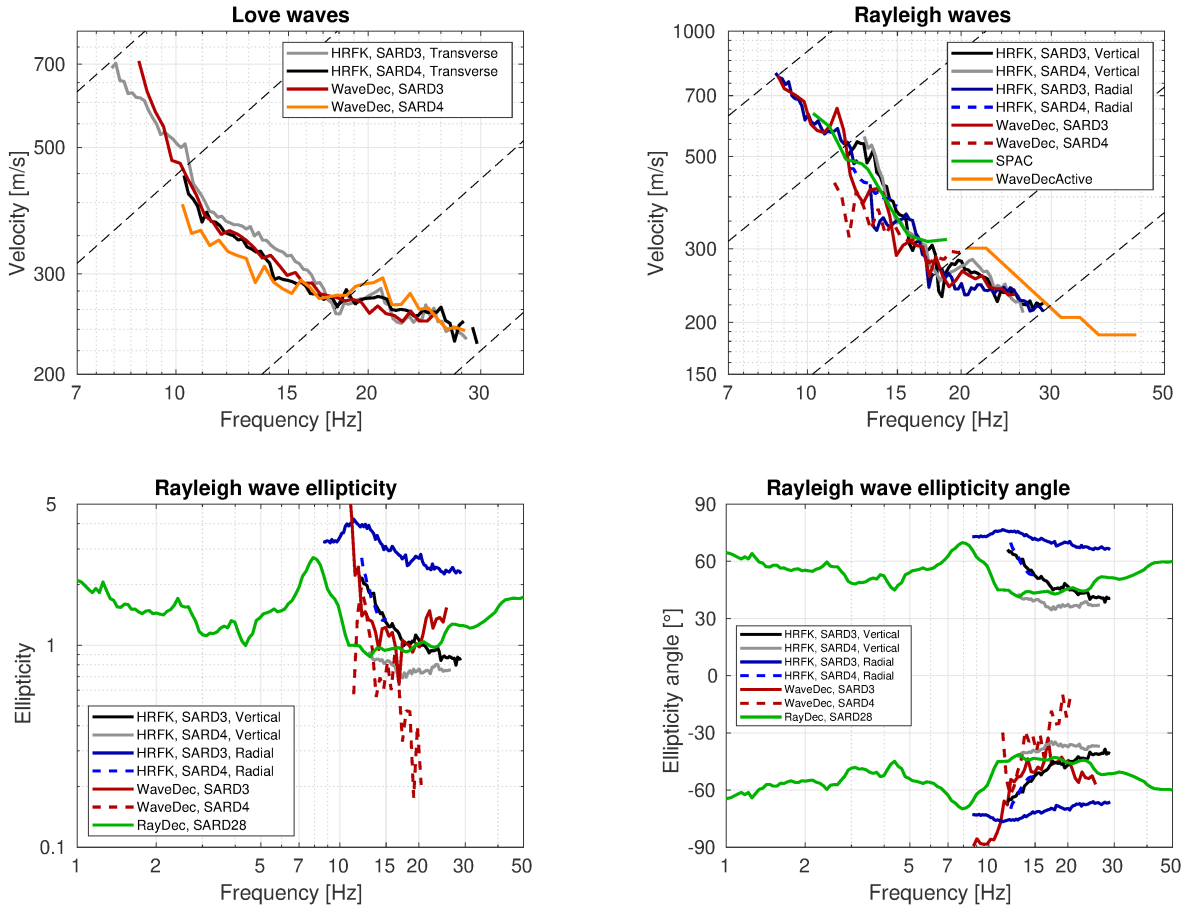

Figure 13: Overview of the Love and Rayleigh wave dispersion curves as well as the ellipticity and ellipticity angle curves for both arrays. The dashed lines indicate the theoretical resolution limits of array 4 (high frequencies) and array 3 (low frequencies). The RayDec ellipticity curve corresponds to station SARD28.

4 Data inversion

4.1 Inversion targets

In order to test if the ellipticity peak at around 8 Hz corresponds to a singularity or not, we defined three different targets for the inversions. In all three inversion targets, the Love and Rayleigh wave dispersion curves were used as targets, combining the results from arrays 3 and 4 to maximize the frequency range. The Rayleigh wave dispersion curve was continued at high frequencies by the WaveDecActive curve. As this one was picked without uncertainties, a slowness error of 0.001 s/m was assumed.
Concerning the ellipticity information, the first target did not include any ellipticity constraints. The second target included parts of the RayDec curve above and below the 8 Hz ellipticity peak, assuming retrograde particle motion below and prograde particle motion above. The third target uses a larger part of the RayDec curve, assuming retrograde particle motion over the whole frequency range, i.e. without singularity.
The details of the inversion targets are indicated in Table 2 and the corresponding curves are shown in Fig. 14.

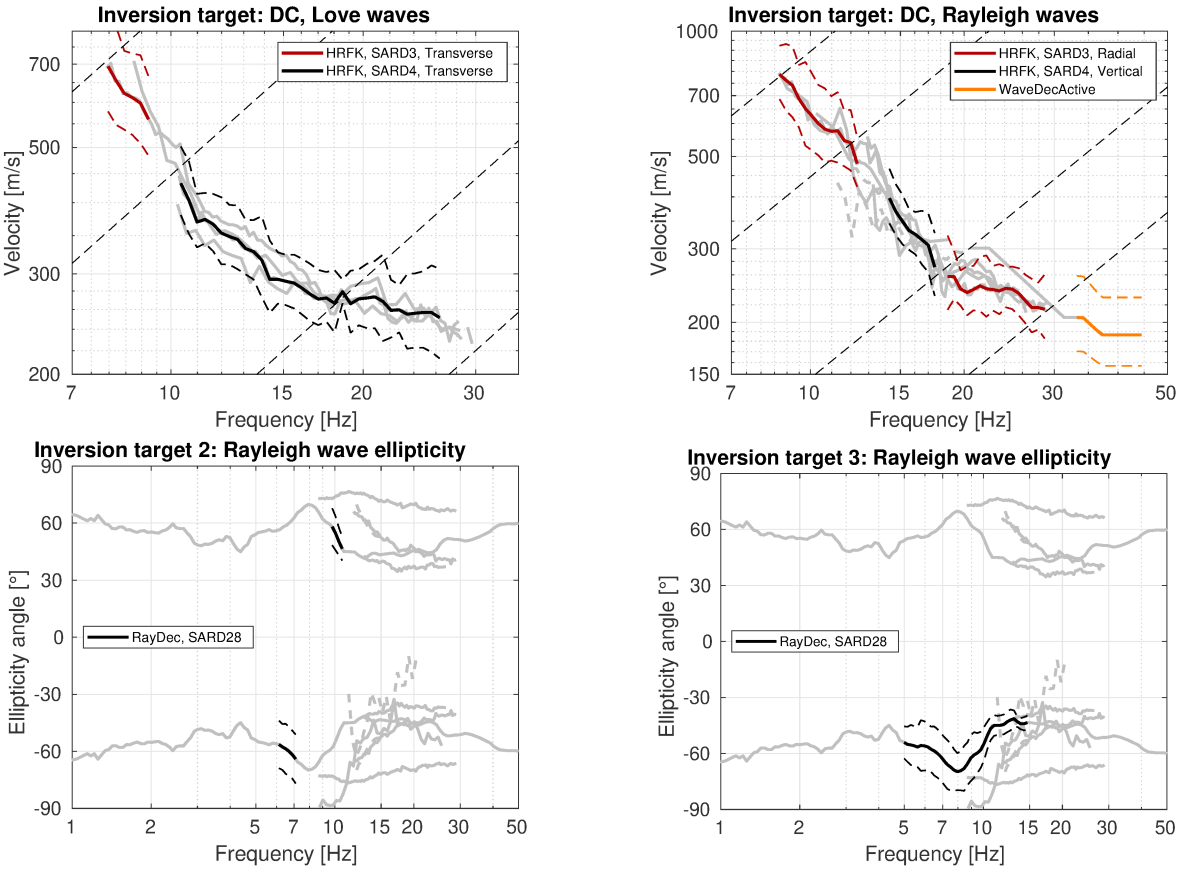

Figure 14: Overview of the dispersion (top) and ellipticity angle (bottom) curves used as targets for the different inversions.

Table 2: List of the different data curves used as target in the different inversions.

Target	Array	Method	Wave type	Mode	Curve type	Frequency range [Hz]
1, 2, 3	3	HRFK (T)	Love	fundamental	dispersion	7.97 - 9.23
1, 2, 3	4	HRFK (T)	Love	fundamental	dispersion	10.36 - 26.34
1, 2, 3	3	HRFK (R)	Rayleigh	fundamental	dispersion	8.69 - 12.71
1, 2, 3	4	HRFK (V)	Rayleigh	fundamental	dispersion	14.27 - 17.51
1, 2, 3	3	HRFK (R)	Rayleigh	fundamental	dispersion	18.02 - 28.74
1, 2, 3		WaveDecActive	Rayleigh	fundamental	dispersion	32.29 - 43.22
2		RayDec (SARD28)	Rayleigh	fundamental	ellipticity angle (-)	6.13 - 7.10
2		RayDec (SARD28)	Rayleigh	fundamental	ellipticity angle (+)	9.77 - 10.67
3		RayDec (SARD28)	Rayleigh	fundamental	ellipticity angle (-)	5.00 - 14.71

4.2 Inversion parameterization

For the inversion, six different parameterizations have been used in total. The first five had free values of the depths and velocities of the different layers, ranging from four to eight layers (including half-space). The last parameterization had fixed layer depths and consisted of 21 layers in total. The P-wave velocities were allowed to vary up to 5000 m/s. The S-wave velocities were allowed to range from 50 to 3500 m/s. The deepest boundaries were parameterized to range to a depth of 100 m maximum. The density was fixed to 2 300 kg/m^3 for the lowest layer, to 1 900 kg/m^3 for the superficial layer (or the first three layers in the fixed-layer case) and to 2 100 kg/m^3 for all other layers. No low-velocity zones were allowed.

4.3 Inversion results

We performed six inversions with different parameterizations for each target. For each parameterization, 20 different runs were performed, but only the one giving the best minimum misfit was kept. In Table 3, the obtained minimum misfit values for these inversions are shown. In order to assure a good convergence of the solution, each inversion run for the 4-layer parameterization produced around 100 000 total models, for 5- to 7-layer parameterizations around 150 000 models and for the 8-layer and the fixed-depth inversions around 200 000 models. The results of the inversions SARD4l1 to SARDfix1 of target 1 are shown in Figs 15 - 20, for the inversions SARD4l2 to SARDfix2 using target 2 in Figs 21 - 26 and for the inversions SARD4l3 to SARDfix3 using target 3 in Figs 27 - 32. The different inversions using target 1 and free layer depths yield identical minimum misfit values and fit the dispersion data in a perfect way. The fixed-depth inversion in this case even has a lower misfit value because the P-wave velocities had more liberty in this inversion, leading to less realistic solutions.
The inversions using target 2 succeed in finding an ellipticity singularity around 8 Hz, which is caused by a strong velocity contrast at around 10 m depth, but fail in fitting the dispersion curves at the same time. Especially the Love wave dispersion curve below 10 Hz is poorly fitted. Also for the Rayleigh wave dispersion curve, discrepancies are observed.

Using target 3, the ellipticity angle is well fitted for all parameterizations, the Love wave dispersion curve is badly fitted below 10 Hz, but well fitted above, and the Rayleigh wave dispersion curve is relatively well fitted. For targets 2 and 3, the fixed-depth approach results in larger misfit values, probably because the interface depths are not fixed in an optimal way.

Table 3: List of inversions

Inversion	Number of layers	Number of models	Minimum misfit
SARD4l1	4	100 025	0.255
SARD5l1	5	149 996	0.255
SARD6l1	6	150 031	0.255
SARD7l1	7	150 008	0.255
SARD8l1	8	200 054	0.255
SARDfix1	21	200 028	0.218
SARD4l2	4	100 027	0.717
SARD5l2	5	150 002	0.764
SARD6l2	6	150 010	0.832
SARD7l2	7	150 005	0.769
SARD8l2	8	200 025	0.720
SARDfix2	21	200 004	1.183
SARD4l3	4	100 019	0.478
SARD5l3	5	150 048	0.453
SARD6l3	6	150 069	0.491
SARD7l3	7	150 008	0.486
SARD8l3	8	200 075	0.477
SARDfix3	21	200 044	0.558

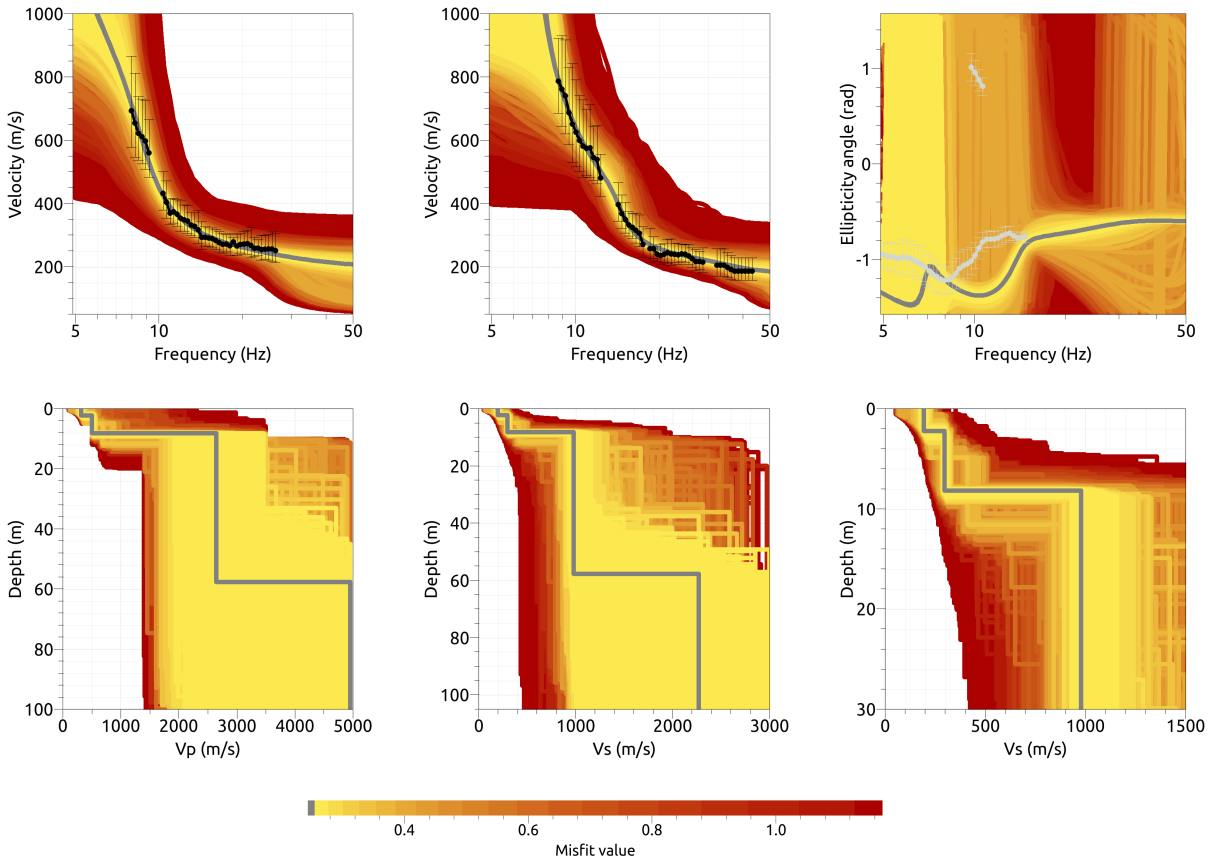

Figure 15: Inversion SARD4l1. Top line: Dispersion curves for Love waves (left) and Rayleigh waves (center) and Rayleigh wave ellipticity angle (right) of the respective fundamental modes. Bottom line: P-wave velocity profiles (left), S-wave velocity profiles (center and zoom on the upper 30 m on the right). All generated models are plotted on top of each other in the color corresponding to the respective misfit value. The black dots with error bars indicate the data points used for the inversion, the gray line indicates the best-fitting model. In the ellipticity angle plot, the light gray dots and error bars indicate the ellipticity values of targets 2 and 3, which where not used for the inversion here.

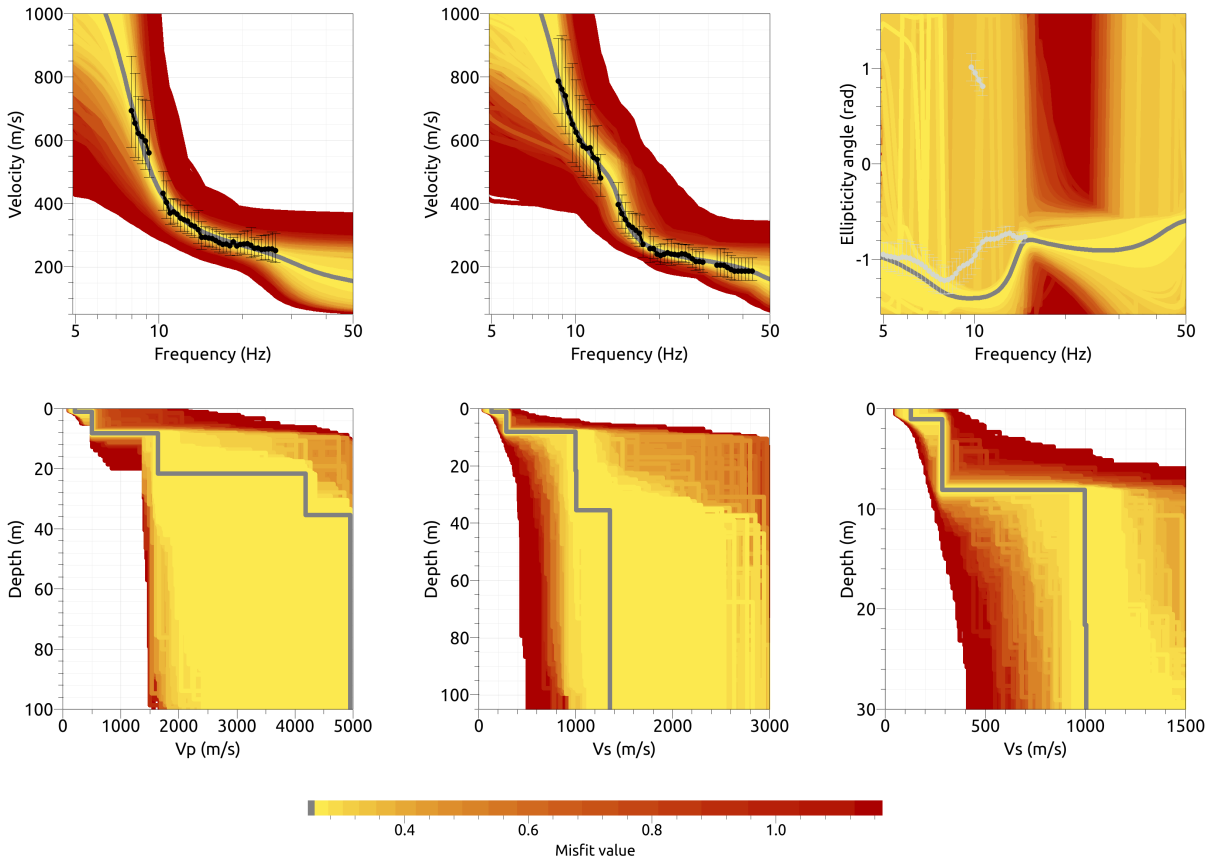

Figure 16: Inversion SARD5l1. Top line: Dispersion curves for Love waves (left) and Rayleigh waves (center) and Rayleigh wave ellipticity angle (right) of the respective fundamental modes. Bottom line: P-wave velocity profiles (left), S-wave velocity profiles (center and zoom on the upper 30 m on the right). All generated models are plotted on top of each other in the color corresponding to the respective misfit value. The black dots with error bars indicate the data points used for the inversion, the gray line indicates the best-fitting model. In the ellipticity angle plot, the light gray dots and error bars indicate the ellipticity values of targets 2 and 3, which where not used for the inversion here.

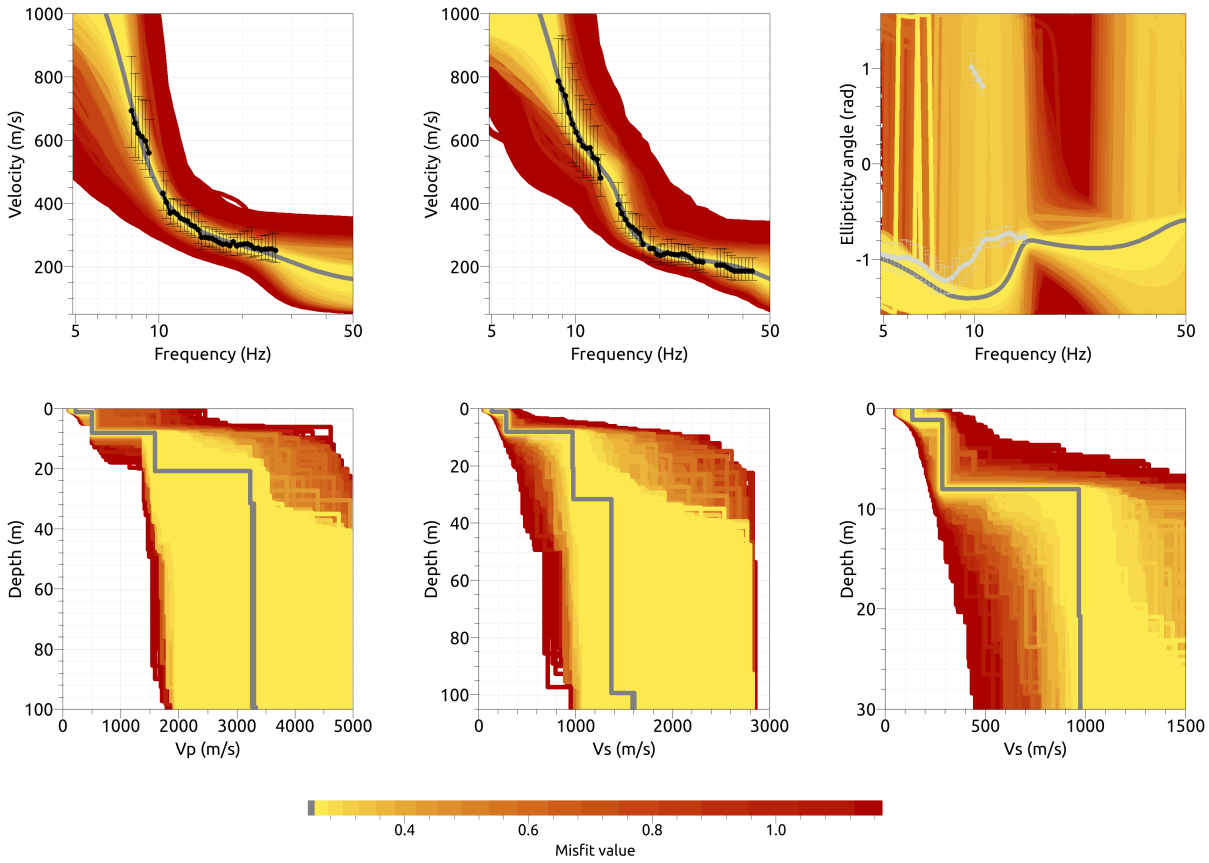

Figure 17: Inversion SARD6l1. Top line: Dispersion curves for Love waves (left) and Rayleigh waves (center) and Rayleigh wave ellipticity angle (right) of the respective fundamental modes. Bottom line: P-wave velocity profiles (left), S-wave velocity profiles (center and zoom on the upper 30 m on the right). All generated models are plotted on top of each other in the color corresponding to the respective misfit value. The black dots with error bars indicate the data points used for the inversion, the gray line indicates the best-fitting model. In the ellipticity angle plot, the light gray dots and error bars indicate the ellipticity values of targets 2 and 3, which where not used for the inversion here.

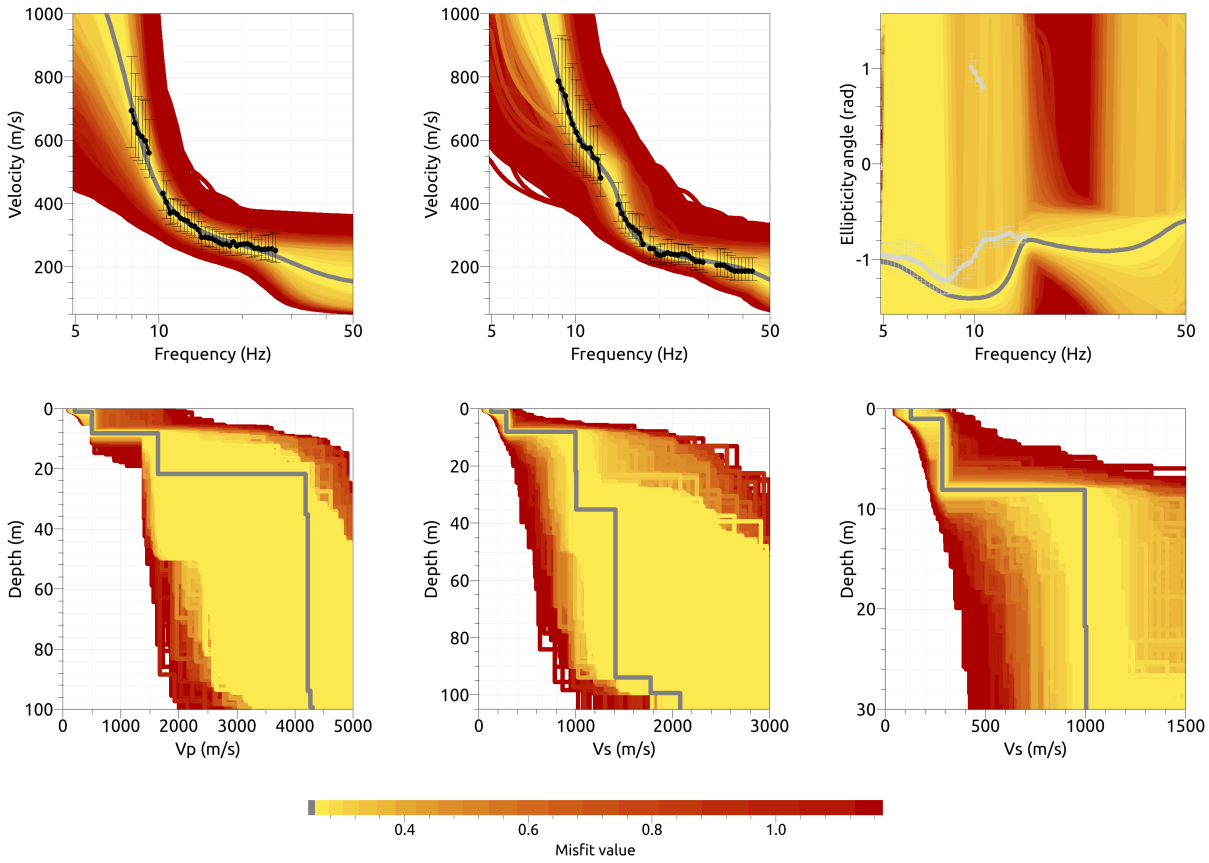

Figure 18: Inversion SARD7l1. Top line: Dispersion curves for Love waves (left) and Rayleigh waves (center) and Rayleigh wave ellipticity angle (right) of the respective fundamental modes. Bottom line: P-wave velocity profiles (left), S-wave velocity profiles (center and zoom on the upper 30 m on the right). All generated models are plotted on top of each other in the color corresponding to the respective misfit value. The black dots with error bars indicate the data points used for the inversion, the gray line indicates the best-fitting model. In the ellipticity angle plot, the light gray dots and error bars indicate the ellipticity values of targets 2 and 3, which where not used for the inversion here.

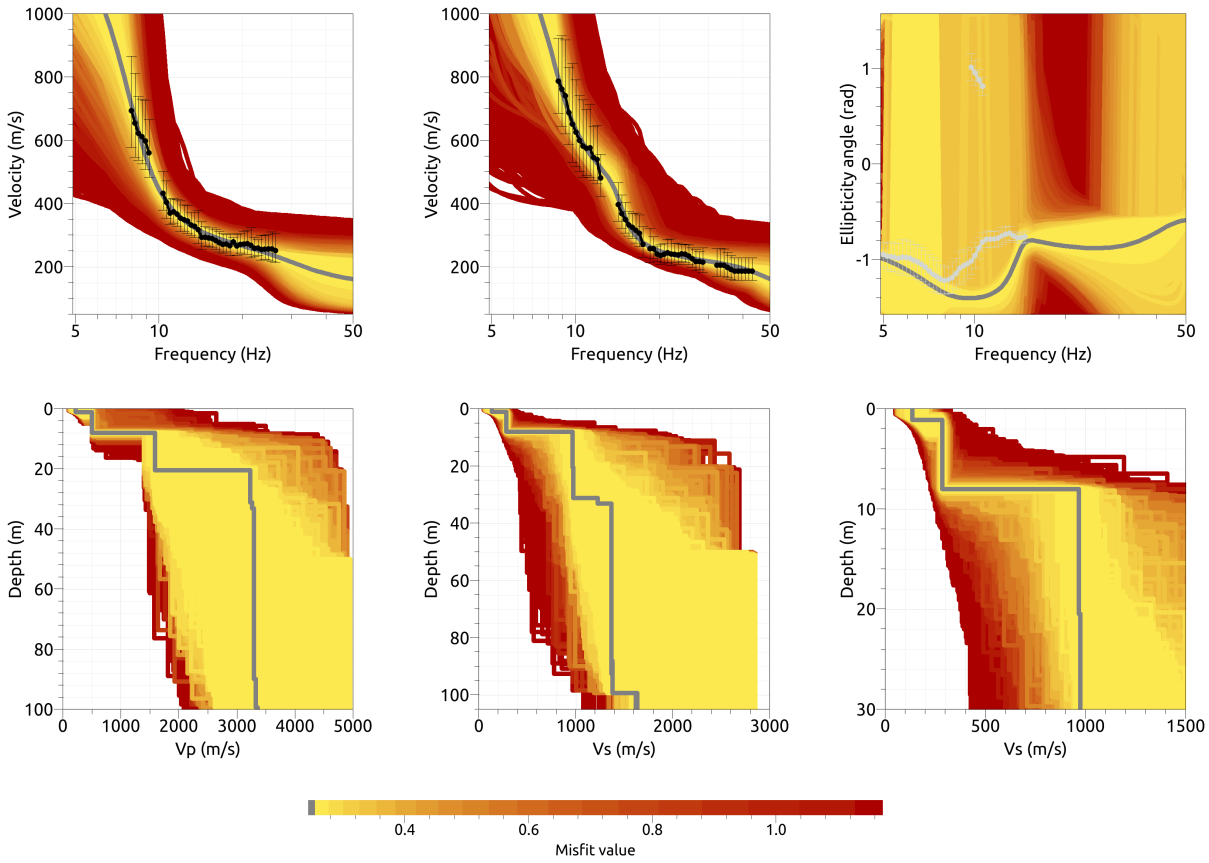

Figure 19: Inversion SARD8l1. Top line: Dispersion curves for Love waves (left) and Rayleigh waves (center) and Rayleigh wave ellipticity angle (right) of the respective fundamental modes. Bottom line: P-wave velocity profiles (left), S-wave velocity profiles (center and zoom on the upper 30 m on the right). All generated models are plotted on top of each other in the color corresponding to the respective misfit value. The black dots with error bars indicate the data points used for the inversion, the gray line indicates the best-fitting model. In the ellipticity angle plot, the light gray dots and error bars indicate the ellipticity values of targets 2 and 3, which where not used for the inversion here.

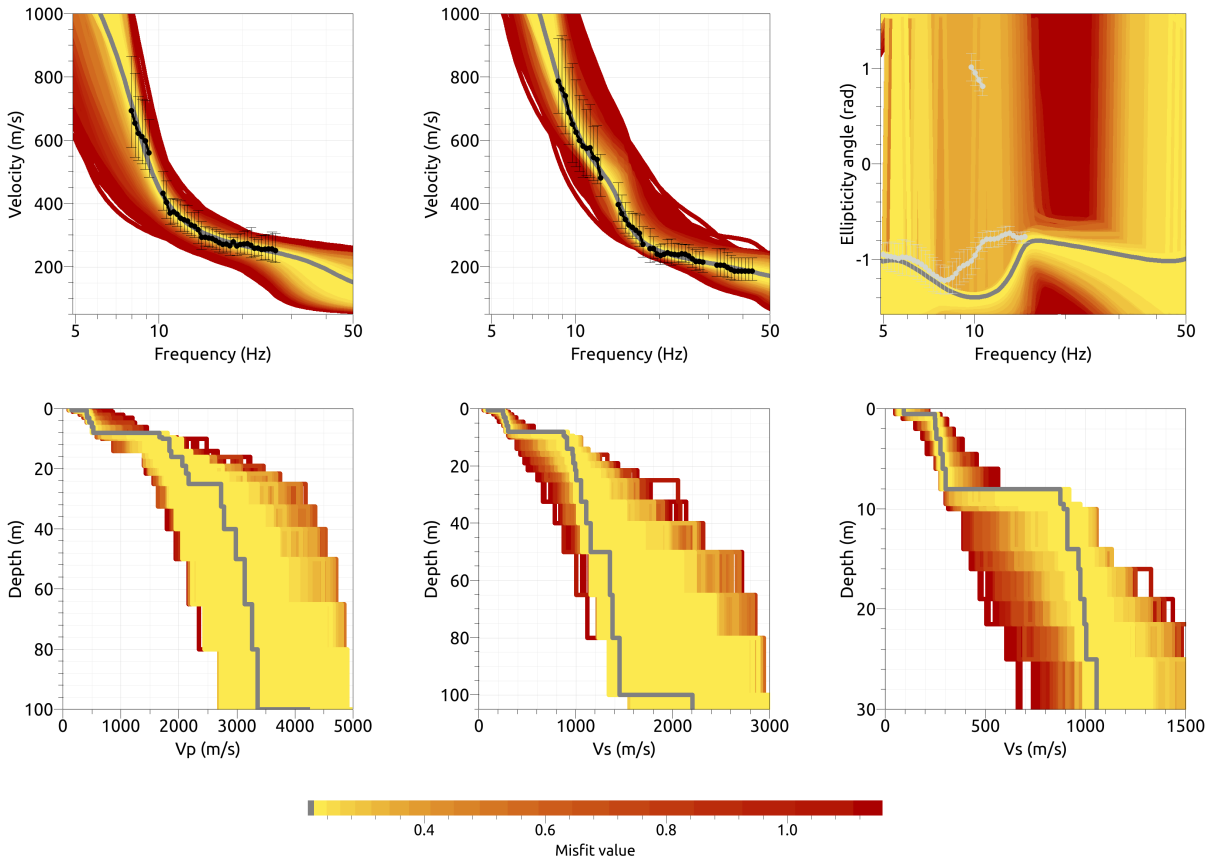

Figure 20: Inversion SARDfix1. Top line: Dispersion curves for Love waves (left) and Rayleigh waves (center) and Rayleigh wave ellipticity angle (right) of the respective fundamental modes. Bottom line: P-wave velocity profiles (left), S-wave velocity profiles (center and zoom on the upper 30 m on the right). All generated models are plotted on top of each other in the color corresponding to the respective misfit value. The black dots with error bars indicate the data points used for the inversion, the gray line indicates the best-fitting model. In the ellipticity angle plot, the light gray dots and error bars indicate the ellipticity values of targets 2 and 3, which where not used for the inversion here.

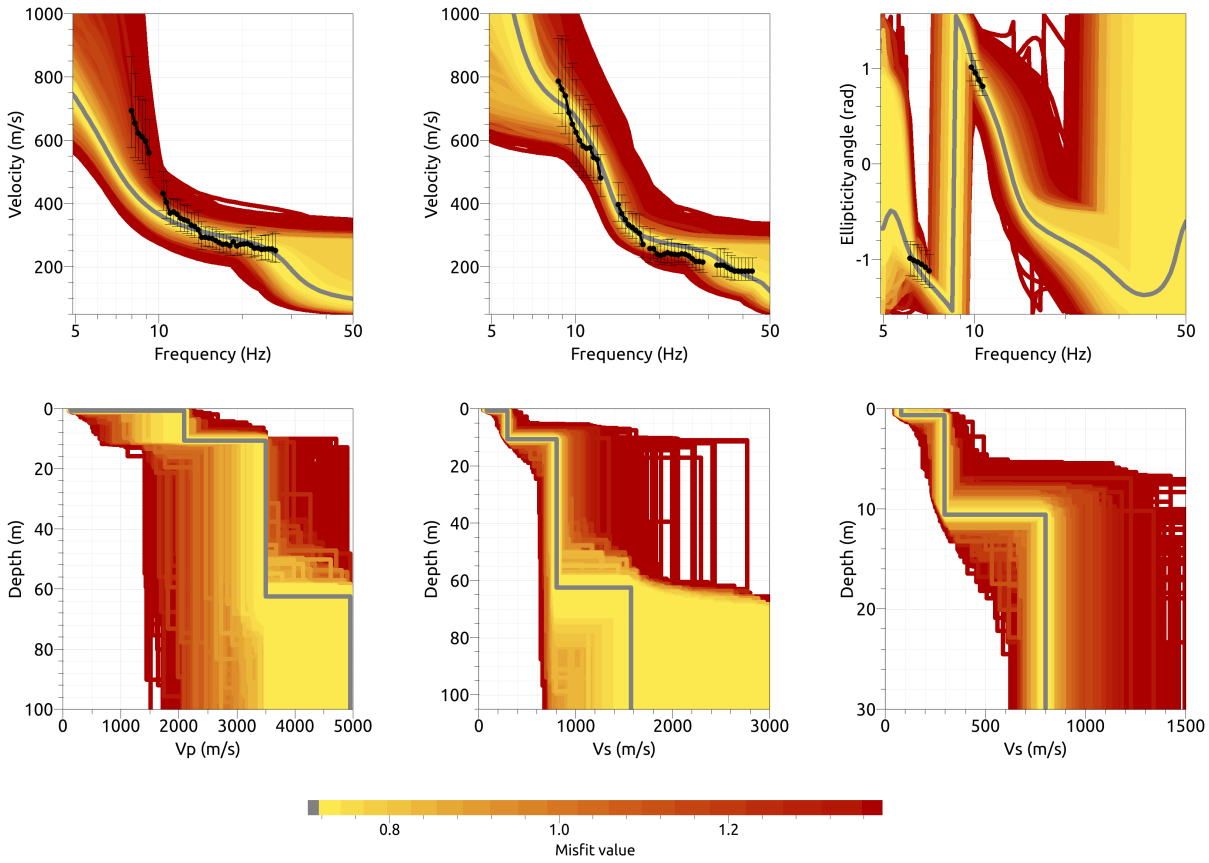

Figure 21: Inversion SARD4l2. Top line: Dispersion curves for Love waves (left) and Rayleigh waves (center) and Rayleigh wave ellipticity angle (right) of the respective fundamental modes. Bottom line: P-wave velocity profiles (left), S-wave velocity profiles (center and zoom on the upper 30 m on the right). All generated models are plotted on top of each other in the color corresponding to the respective misfit value. The black dots with error bars indicate the data points used for the inversion, the gray line indicates the best-fitting model.

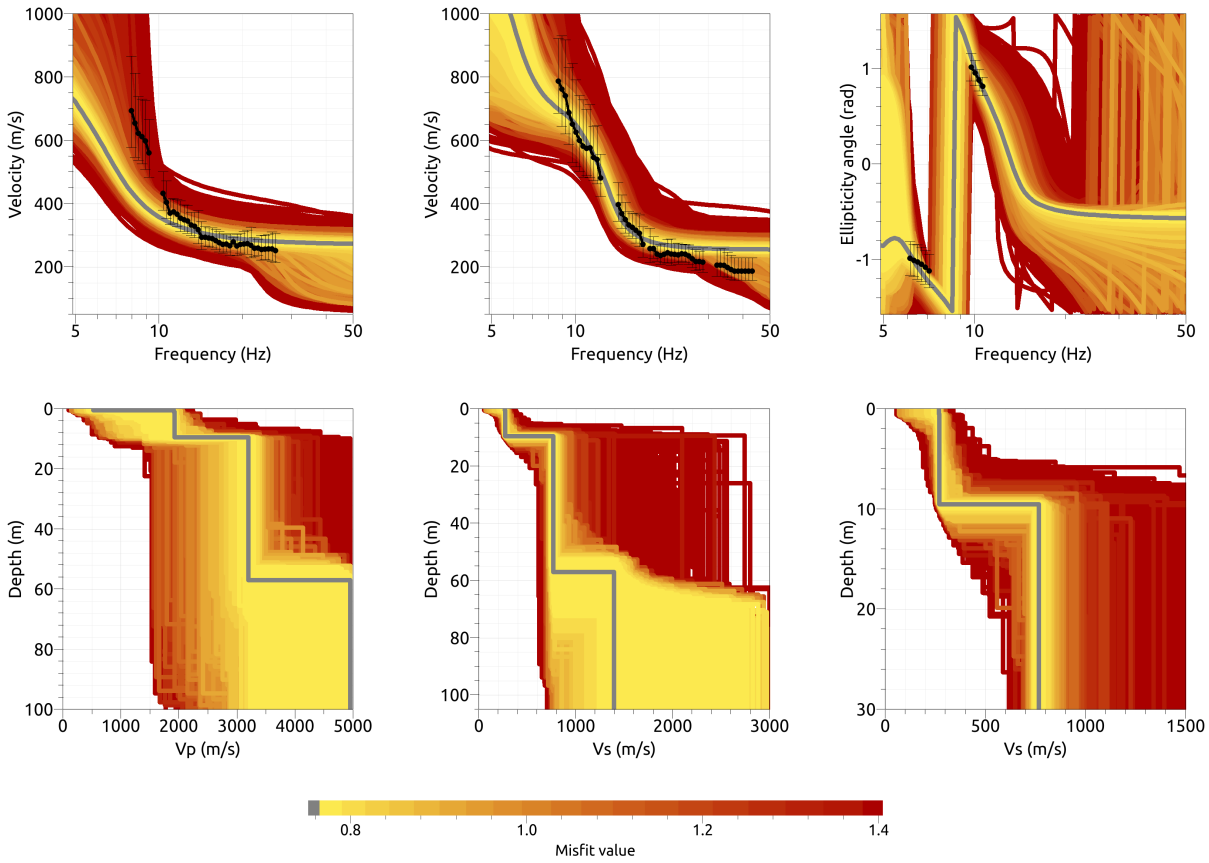

Figure 22: Inversion SARD5l2. Top line: Dispersion curves for Love waves (left) and Rayleigh waves (center) and Rayleigh wave ellipticity angle (right) of the respective fundamental modes. Bottom line: P-wave velocity profiles (left), S-wave velocity profiles (center and zoom on the upper 30 m on the right). All generated models are plotted on top of each other in the color corresponding to the respective misfit value. The black dots with error bars indicate the data points used for the inversion, the gray line indicates the best-fitting model.

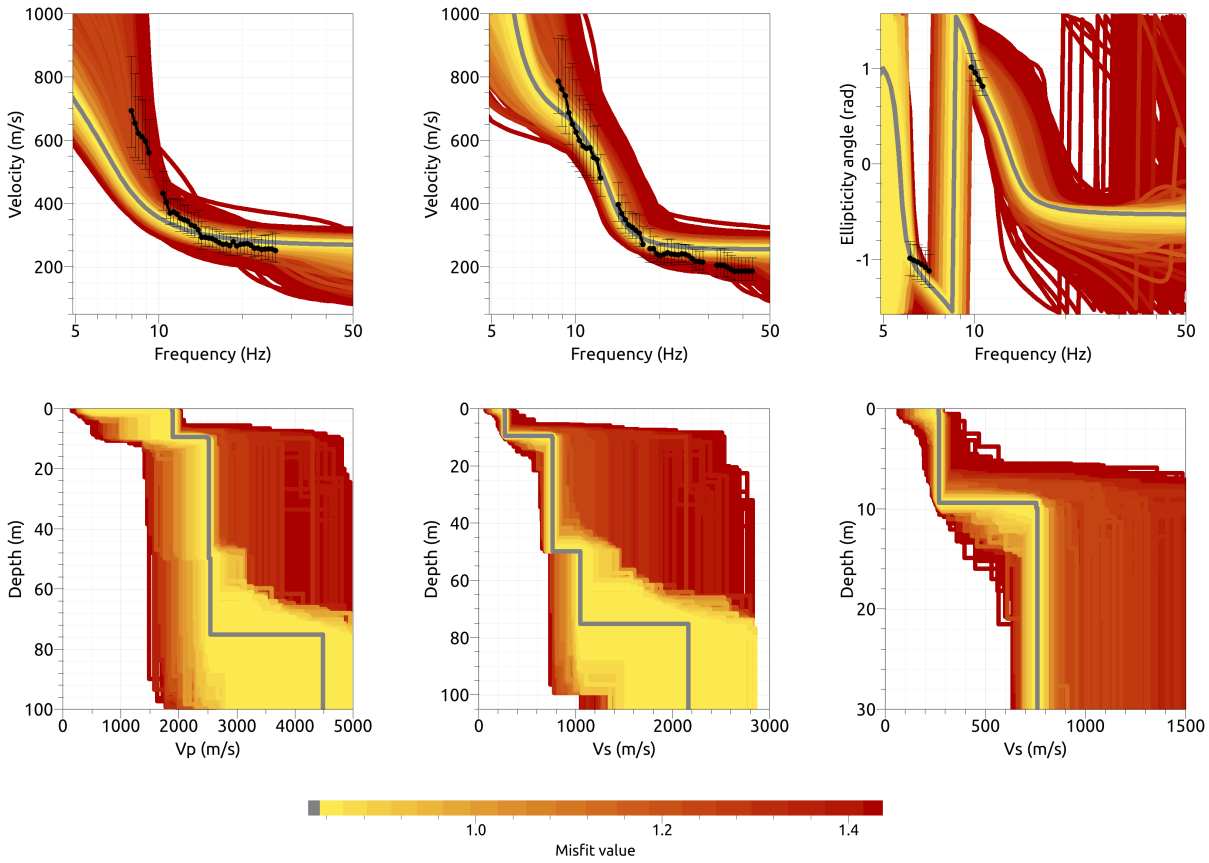

Figure 23: Inversion SARD6l2. Top line: Dispersion curves for Love waves (left) and Rayleigh waves (center) and Rayleigh wave ellipticity angle (right) of the respective fundamental modes. Bottom line: P-wave velocity profiles (left), S-wave velocity profiles (center and zoom on the upper 30 m on the right). All generated models are plotted on top of each other in the color corresponding to the respective misfit value. The black dots with error bars indicate the data points used for the inversion, the gray line indicates the best-fitting model.

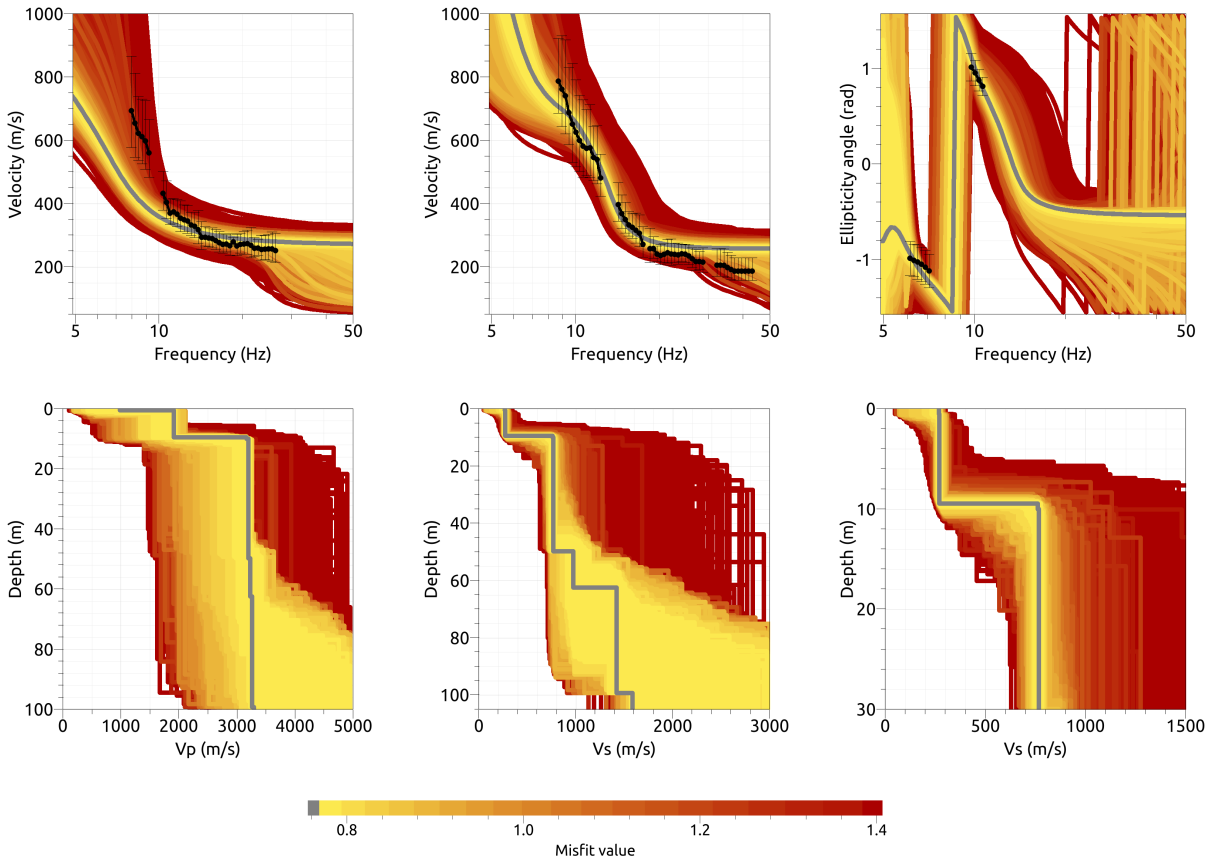

Figure 24: Inversion SARD7l2. Top line: Dispersion curves for Love waves (left) and Rayleigh waves (center) and Rayleigh wave ellipticity angle (right) of the respective fundamental modes. Bottom line: P-wave velocity profiles (left), S-wave velocity profiles (center and zoom on the upper 30 m on the right). All generated models are plotted on top of each other in the color corresponding to the respective misfit value. The black dots with error bars indicate the data points used for the inversion, the gray line indicates the best-fitting model.

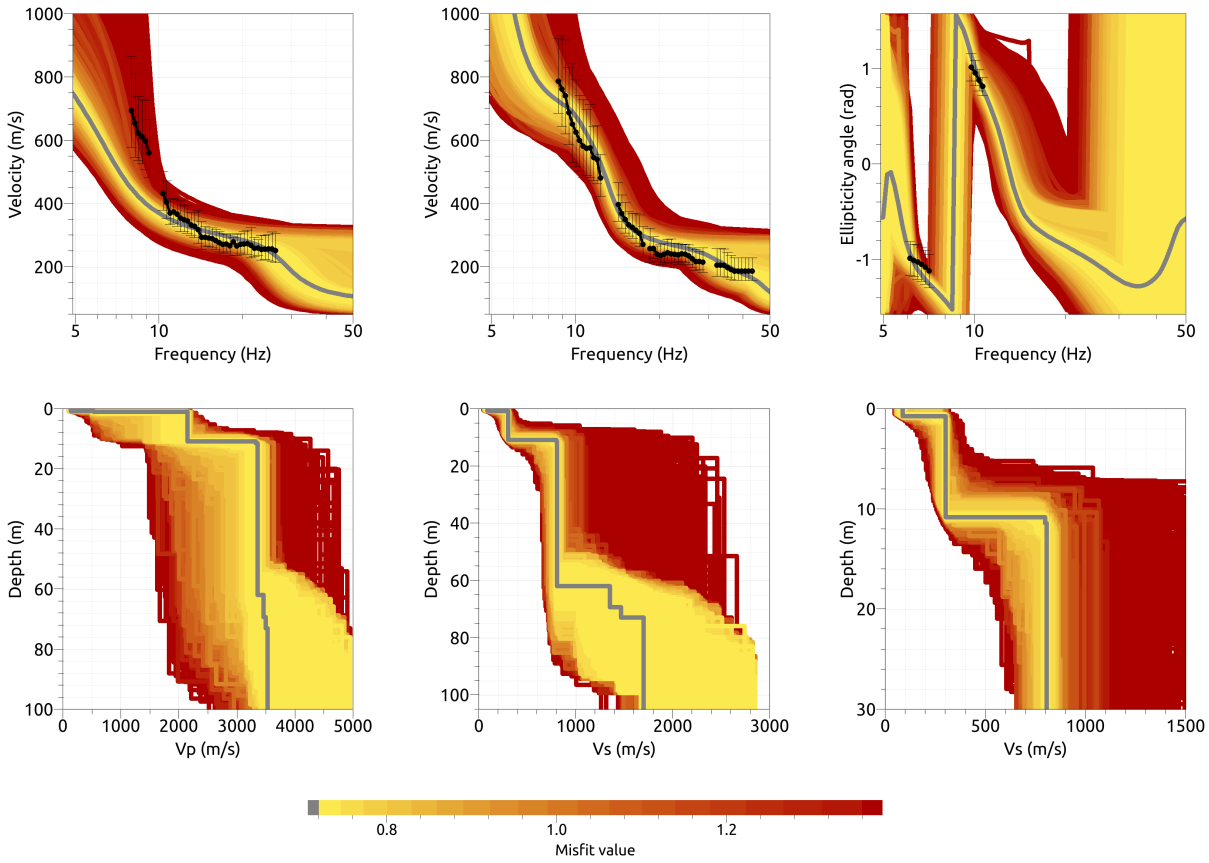

Figure 25: Inversion SARD8l2. Top line: Dispersion curves for Love waves (left) and Rayleigh waves (center) and Rayleigh wave ellipticity angle (right) of the respective fundamental modes. Bottom line: P-wave velocity profiles (left), S-wave velocity profiles (center and zoom on the upper 30 m on the right). All generated models are plotted on top of each other in the color corresponding to the respective misfit value. The black dots with error bars indicate the data points used for the inversion, the gray line indicates the best-fitting model.

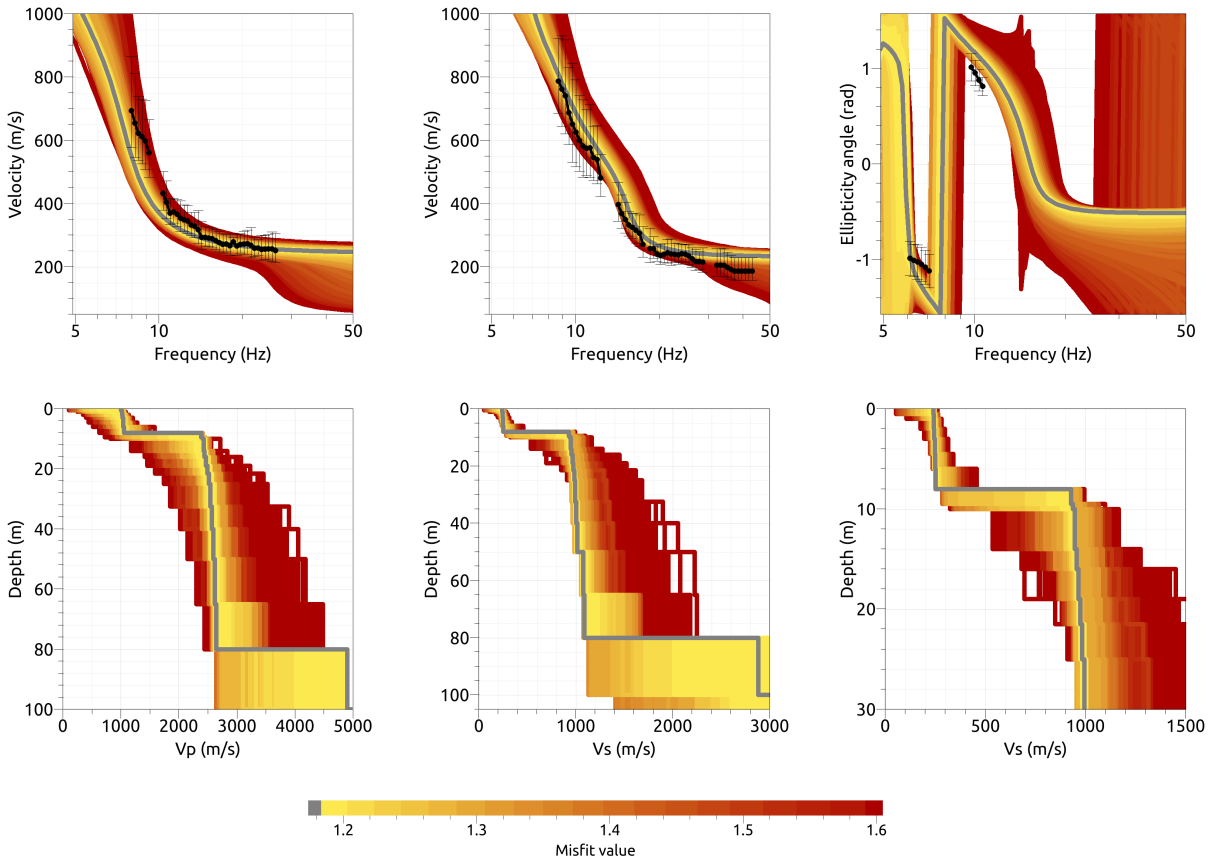

Figure 26: Inversion SARDfix2. Top line: Dispersion curves for Love waves (left) and Rayleigh waves (center) and Rayleigh wave ellipticity angle (right) of the respective fundamental modes. Bottom line: P-wave velocity profiles (left), S-wave velocity profiles (center and zoom on the upper 30 m on the right). All generated models are plotted on top of each other in the color corresponding to the respective misfit value. The black dots with error bars indicate the data points used for the inversion, the gray line indicates the best-fitting model.

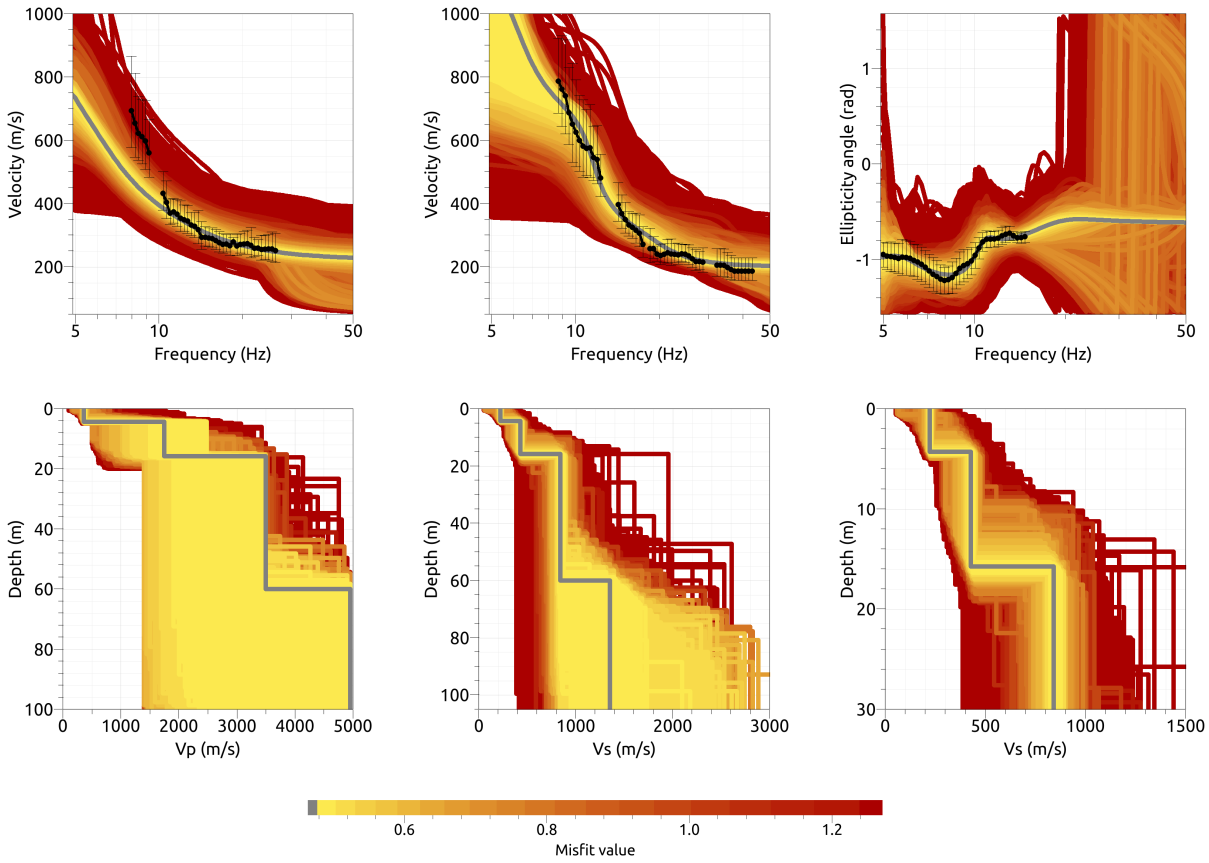

Figure 27: Inversion SARD4l3. Top line: Dispersion curves for Love waves (left) and Rayleigh waves (center) and Rayleigh wave ellipticity angle (right) of the respective fundamental modes. Bottom line: P-wave velocity profiles (left), S-wave velocity profiles (center and zoom on the upper 30 m on the right). All generated models are plotted on top of each other in the color corresponding to the respective misfit value. The black dots with error bars indicate the data points used for the inversion, the gray line indicates the best-fitting model.

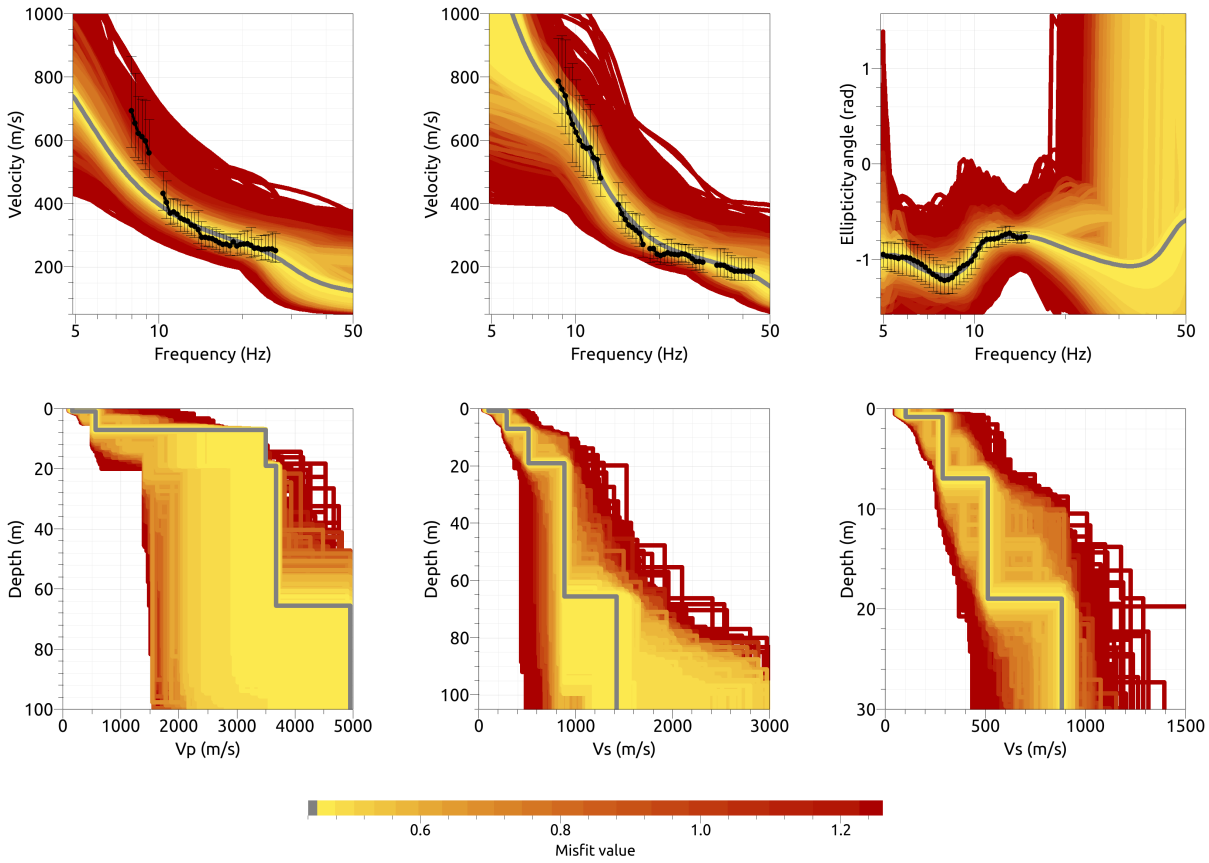

Figure 28: Inversion SARD5l3. Top line: Dispersion curves for Love waves (left) and Rayleigh waves (center) and Rayleigh wave ellipticity angle (right) of the respective fundamental modes. Bottom line: P-wave velocity profiles (left), S-wave velocity profiles (center and zoom on the upper 30 m on the right). All generated models are plotted on top of each other in the color corresponding to the respective misfit value. The black dots with error bars indicate the data points used for the inversion, the gray line indicates the best-fitting model.

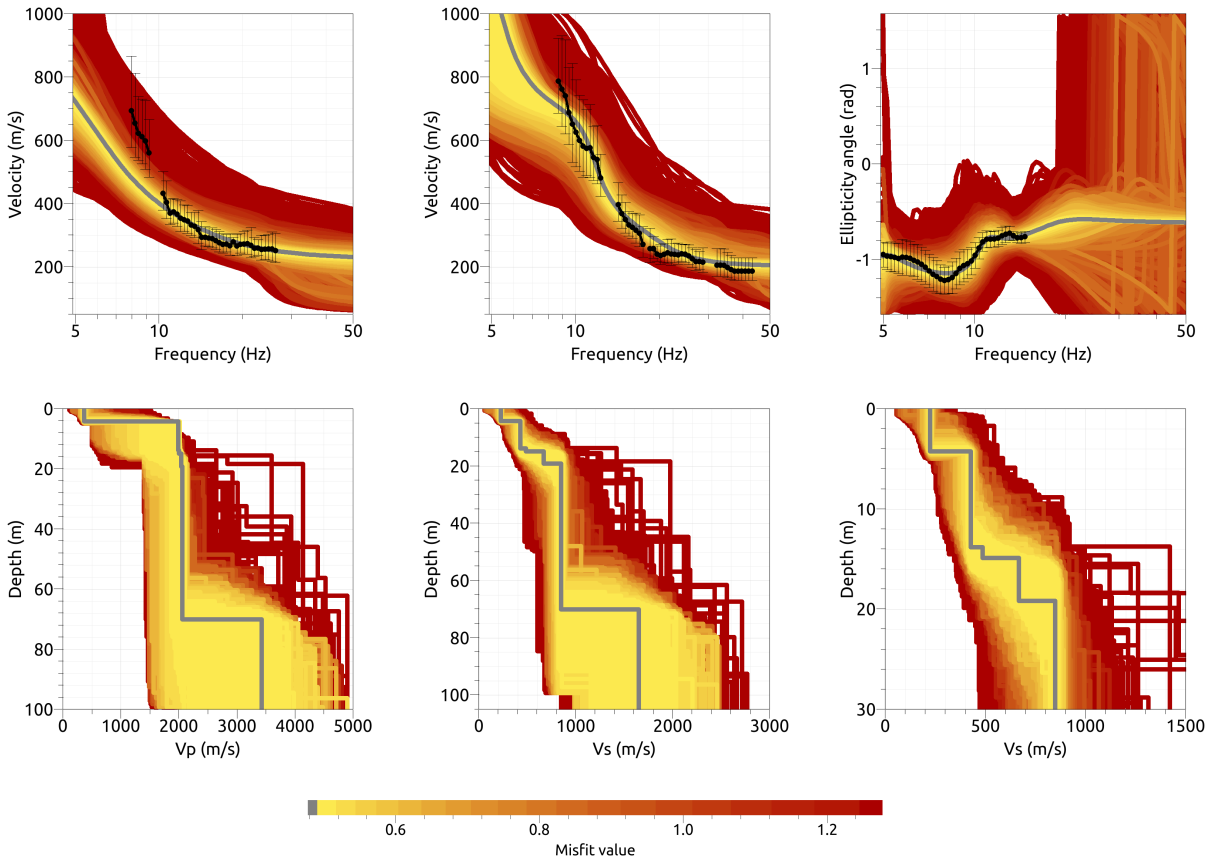

Figure 29: Inversion SARD6l3. Top line: Dispersion curves for Love waves (left) and Rayleigh waves (center) and Rayleigh wave ellipticity angle (right) of the respective fundamental modes. Bottom line: P-wave velocity profiles (left), S-wave velocity profiles (center and zoom on the upper 30 m on the right). All generated models are plotted on top of each other in the color corresponding to the respective misfit value. The black dots with error bars indicate the data points used for the inversion, the gray line indicates the best-fitting model.

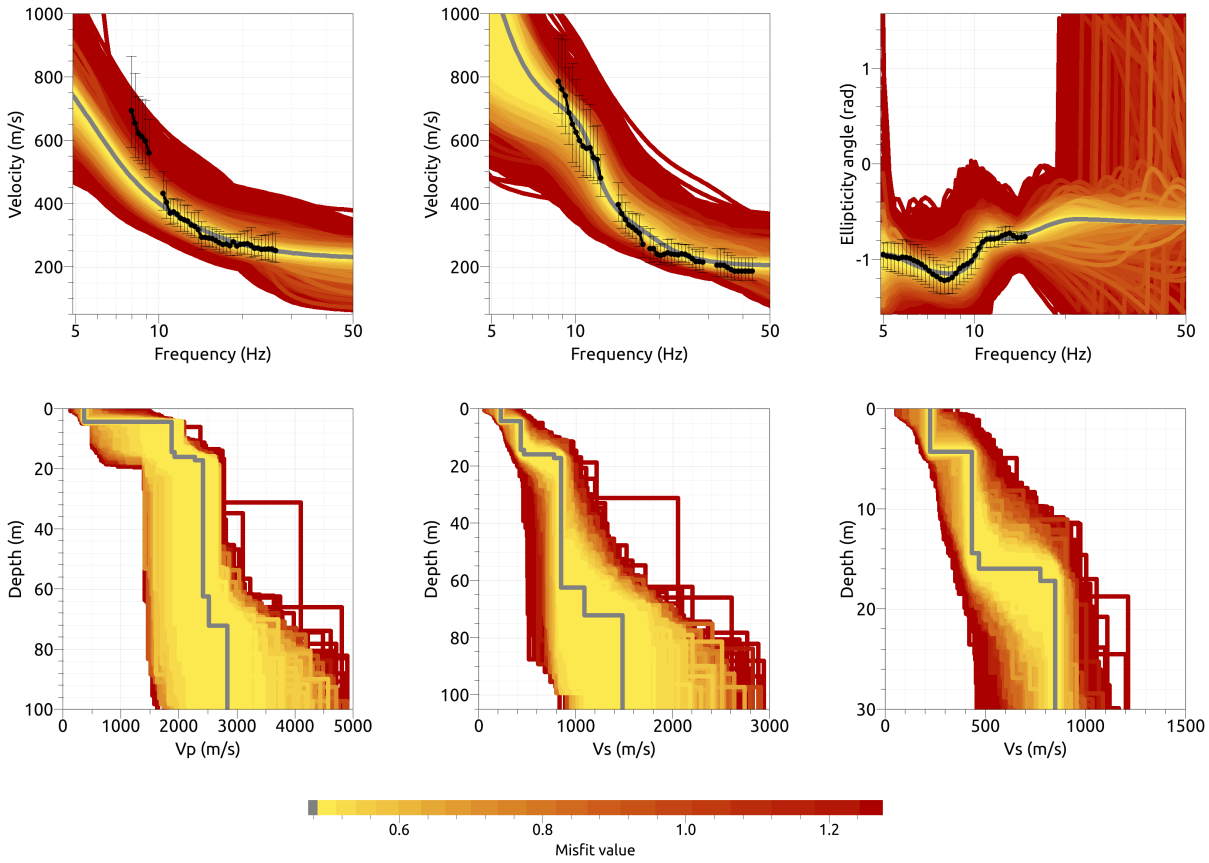

Figure 30: Inversion SARD7l3. Top line: Dispersion curves for Love waves (left) and Rayleigh waves (center) and Rayleigh wave ellipticity angle (right) of the respective fundamental modes. Bottom line: P-wave velocity profiles (left), S-wave velocity profiles (center and zoom on the upper 30 m on the right). All generated models are plotted on top of each other in the color corresponding to the respective misfit value. The black dots with error bars indicate the data points used for the inversion, the gray line indicates the best-fitting model.

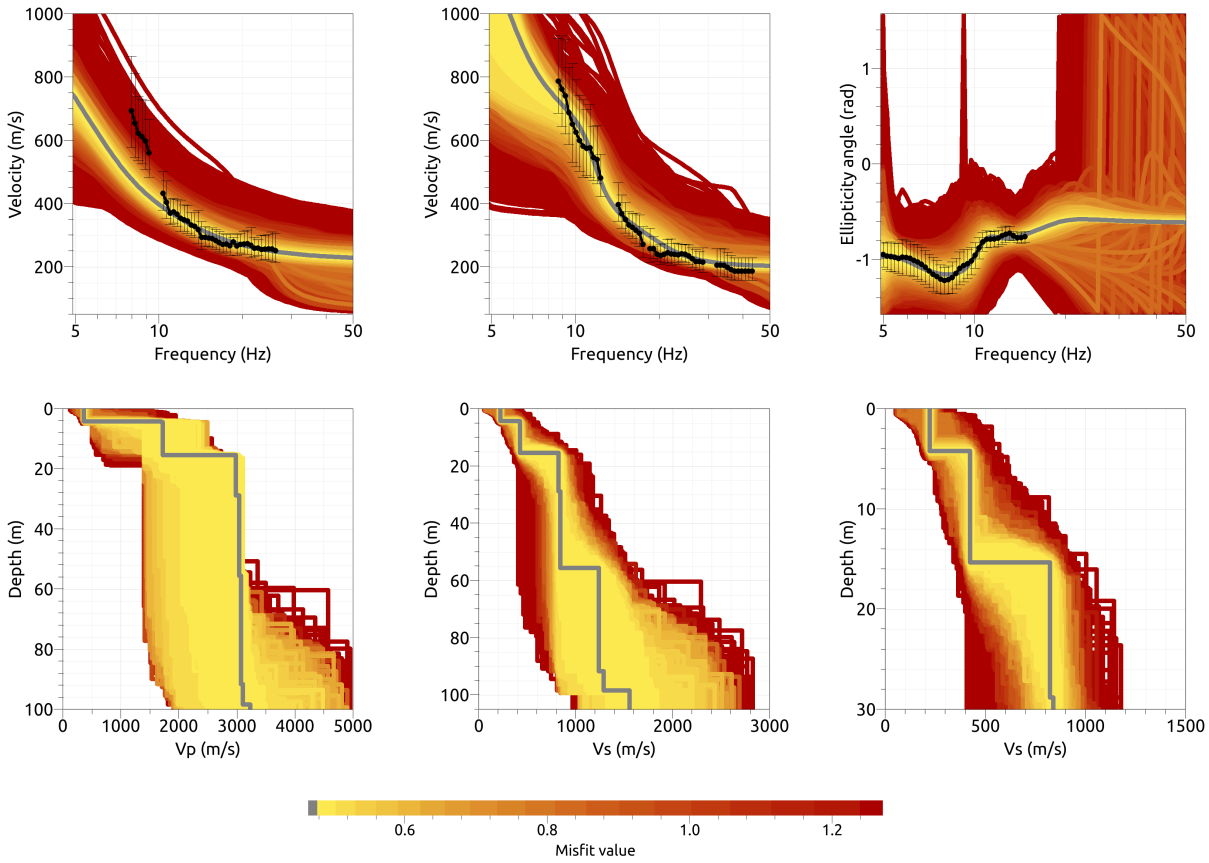

Figure 31: Inversion SARD8l3. Top line: Dispersion curves for Love waves (left) and Rayleigh waves (center) and Rayleigh wave ellipticity angle (right) of the respective fundamental modes. Bottom line: P-wave velocity profiles (left), S-wave velocity profiles (center and zoom on the upper 30 m on the right). All generated models are plotted on top of each other in the color corresponding to the respective misfit value. The black dots with error bars indicate the data points used for the inversion, the gray line indicates the best-fitting model.

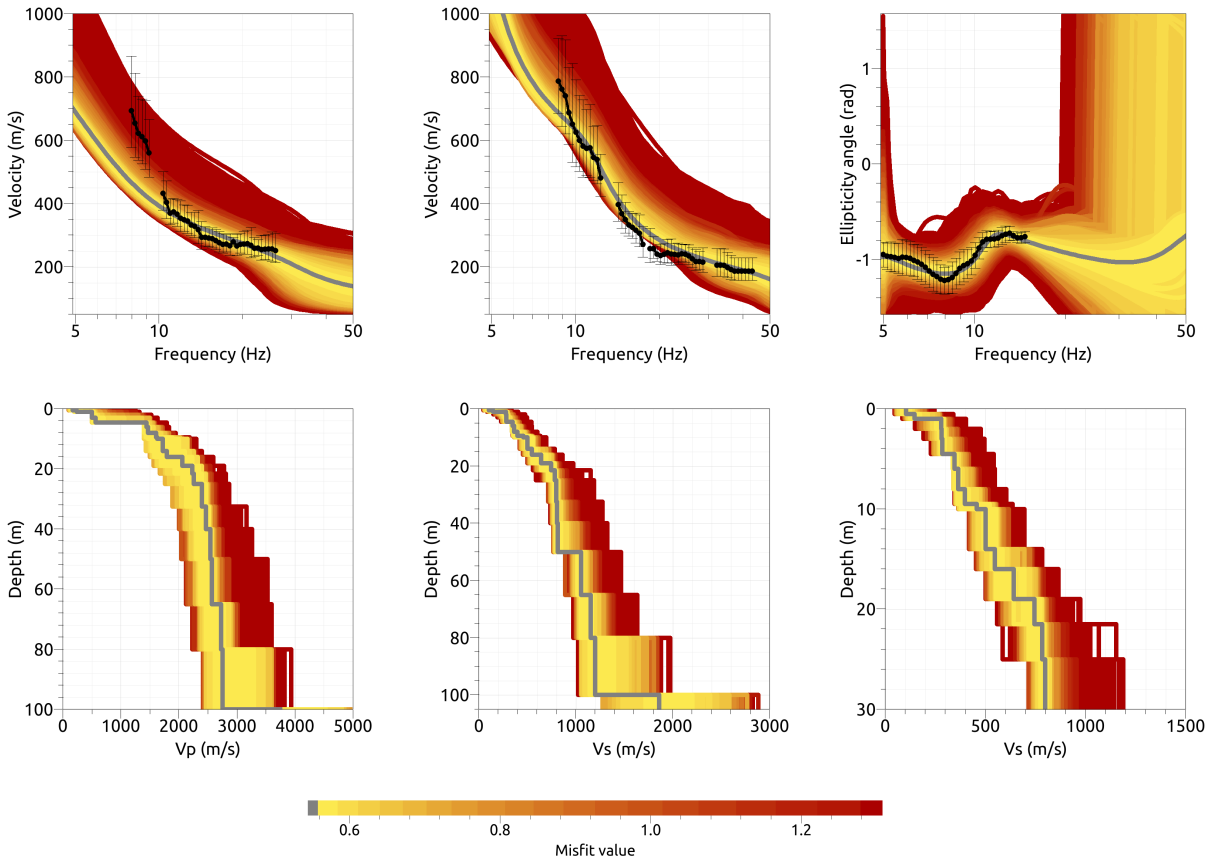

Figure 32: Inversion SARDfix3. Top line: Dispersion curves for Love waves (left) and Rayleigh waves (center) and Rayleigh wave ellipticity angle (right) of the respective fundamental modes. Bottom line: P-wave velocity profiles (left), S-wave velocity profiles (center and zoom on the upper 30 m on the right). All generated models are plotted on top of each other in the color corresponding to the respective misfit value. The black dots with error bars indicate the data points used for the inversion, the gray line indicates the best-fitting model.

4.4 Overview of the inversion result

The best-fitting models of all inversions are shown in Fig. 33. Using target 1, i.e. without using the ellipticity information, we find models with a near-surface shear-wave velocity between 90 and 200 m/s, increasing to velocities between 250 and 300 m/s at depths between around 1 and 8 m. All models show a strong velocity contrast between 8.0 and 8.2 m of depth, where the velocity increases to over 960 m/s. Below, the velocity increases more gradually.
Using target 2, i.e. forcing an ellipticity singularity, the different models are more different. Some parameterizations find a 0.7 m thick layer with a shear-wave velocity around 70 m/s at the surface, while other models fix the velocity there to 240 to 270 m/s. All models have velocities ranging from 240 to 300 m/s between 0.7 and 8.0 m depth, where a strong velocity contrast is found with an increase of velocity to over 750 m/s. The thickness of the contrast ranges from 8.0 to 11.0 m for the different models.
For target 3, i.e. forcing the ellipticity not to have a singularity, the model velocities increase more gradually. Most inversions, namely SARD4l3, SARD6l3, SARD7l3 and SARD8l3, find models consisting of a first, 4.2 m thick layer with a shear-wave velocity of around 220 m/s, followed by a velocity increase to 420 to 430 m/s. They find a relatively strong velocity contrast at depths between 15.3 and 16.0 m, with a velocity increase to over 800 m/s. The five-layer inversion SARD5l3, however, which has a slightly lower minimum misfit value, yields a best model which consists of a first 0.8 m thick shallow layer with a shear-wave velocity of around 100 m/s, followed by a layer with 290 m/s down to about 7.0 m, where the velocity increases to around 510 m/s. Another increase to around 890 m/s is found at around 19.0 m depth. The fixed-depth result shows a more gradual velocity increase over the whole profile.
The V_{S30} value for the inversions with target 1 is 546.9 ± 4.7 m/s, 484.6 ± 32.0 m/s for target 2 and 470.3 ± 10.5 m/s for target 3.
In EC8, this corresponds to soil class E for targets 1 and 2 and to soil class B for target 3. In SIA261, all sites would be classified as soil class E.
Based on the minimum misfit values and the inversion results, we disregard the models for target 2 and keep the ones for targets 1 and 3 as representative results for the site. For this ensemble of models, V_{S30} is $508.6 \pm 40.8\, m/s$.

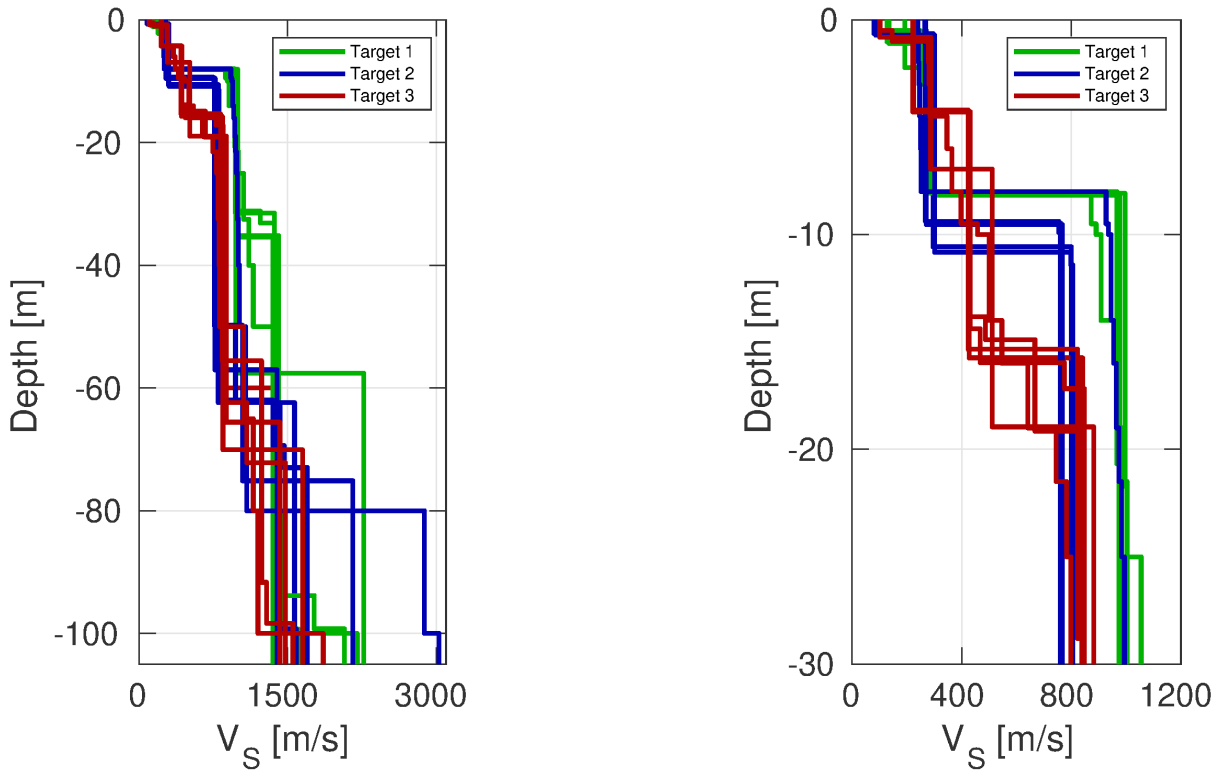

Figure 33: Overview of shear-wave velocity profiles of the best-fitting models of all inversions (left) and a zoom on the shallow part (right).

4.5 Site amplification

In Fig. 34, the theoretical amplification functions for the best models resulting from different parameterizations for the three targets are compared with the empirical amplification for station SARD, based on 47 events so far. The amplification for the inversion models is in good agreement with the empirical amplification around the peak frequency at 8 Hz. At lower frequencies, the empirical curve shows deamplification in contrast to the modeled amplifications. The curve for target 3 shows peaks at frequencies of around 16 and 26 Hz, where the empirical amplification also shows peaks. However, their amplitudes are different.
The bottom plot of Fig. 34 shows a comparision of the empirical amplification and the average amplification of the models for targets 1 and 3, which we accepted as solutions. The different peaks are in good agreement, but differ in amplitude.

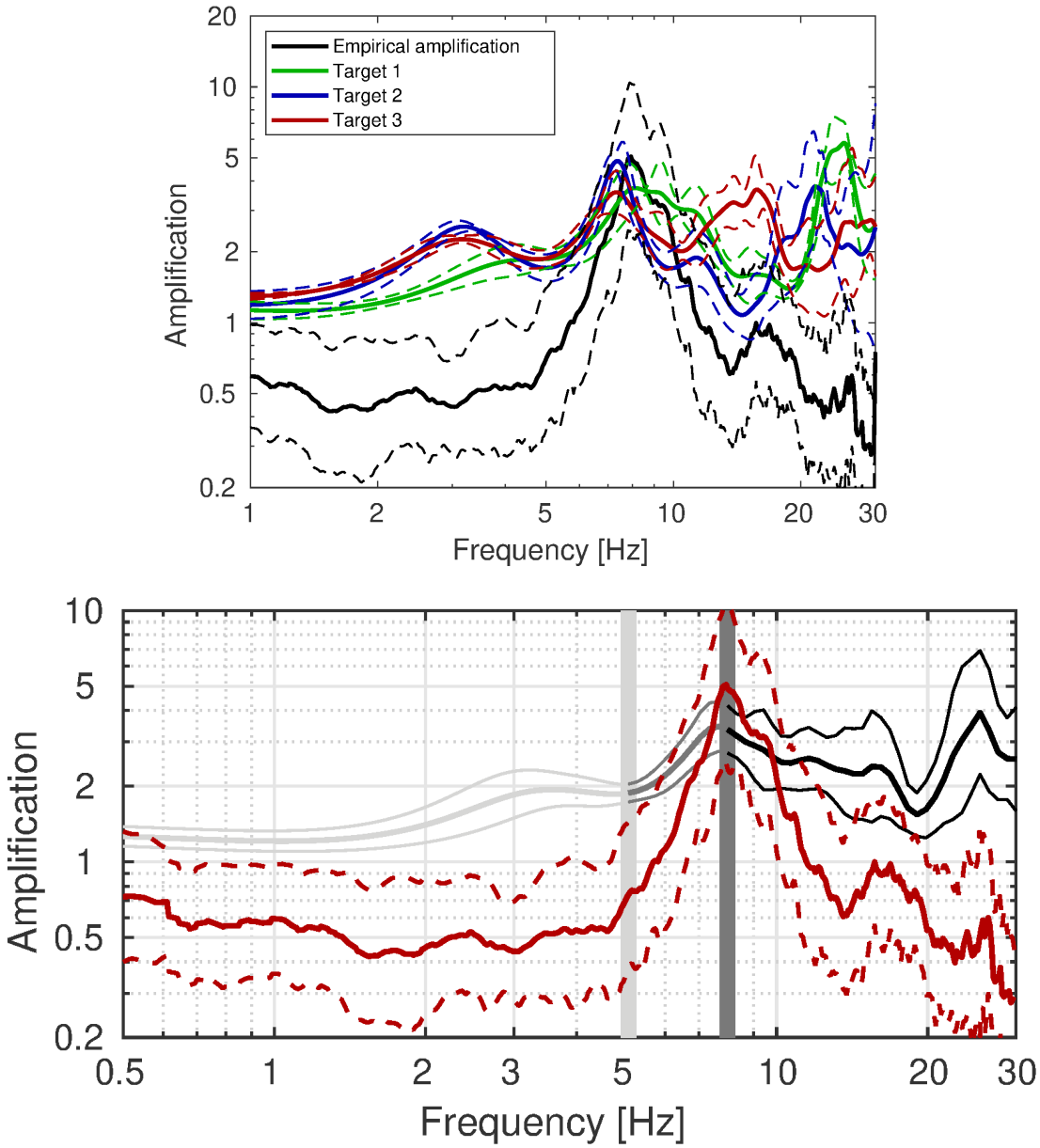

Figure 34: Top: Comparison between the modeled amplification for the best models of the different inversions using targets 1, 2 and 3 (colored curves with standard deviations) and the empirical amplification measured at station SARD (black, with standard deviation). Bottom: Comparison between the modeled amplification for the selected models using targets 1 and 3 (in gray to black, with standard deviation) and the empirical amplification measured at station SARD (red, with standard deviation). The vertical light and dark grey bars correspond to the lowest frequency of the ellipticity and dispersion curves, respectively.

4.6 Quarter-wavelength representation

The quarter-wavelength velocity approach (Joyner et al., 1981) provides, for a given frequency, the average velocity at a depth corresponding to 1/4 of the wavelength of interest. It is useful to identify the frequency limits of the experimental data (the minimum frequency of the dispersion curve used in the inversion is 7.97 Hz, the minimum frequency used for the ellipticity inversion 5.00 Hz). The results using this proxy show that the dispersion curves constrain the profiles down to only about 8.5 m, and to about 20.1 m using the ellipticity information (Fig. 35). Moreover, the quarter wavelength impedance-contrast introduced by Poggi et al. (2012) is also displayed in the figure. It corresponds to the ratio between two quarter-wavelength average velocities, respectively from the top and the bottom part of the velocity profile, at a given frequency (Poggi et al., 2012). This curve shows a strong contrast at the fundamental frequency of the site.

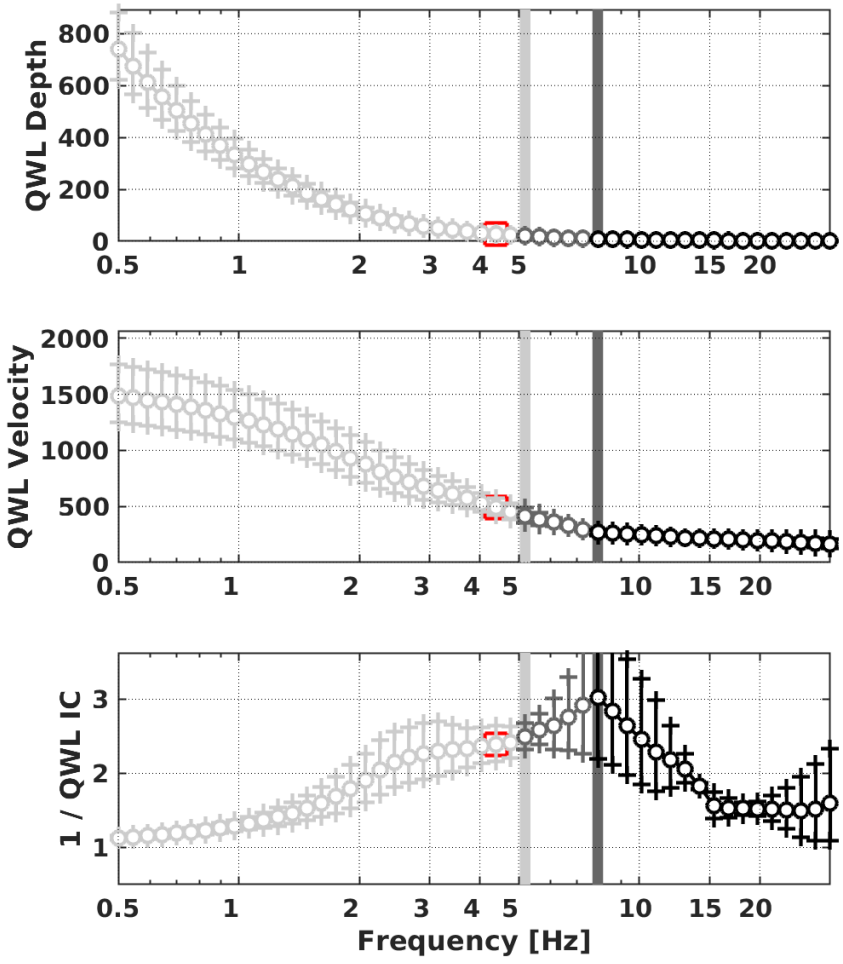

Figure 35: Quarter wavelength representation of the velocity profile for the best models of the inversions (top: depth, center: velocity, bottom: inverse of the impedance contrast). The black curves are constrained by the dispersion curves, the light grey curves are not constrained by the data. The red square corresponds to V_{S30}.

5 Conclusion

We performed a passive array measurement with two arrays to characterize the soil underneath station SARD in Ardez (GR), located on the transition zone between moraine and outcropping dolomite.
We could not retrieve dispersion curves for the two arrays, but only for subarrays of the smaller array. The dispersion curves for Love and Rayleigh waves could be measured between 7.9 to 30 Hz for Love waves and from 8.6 to 44.1 Hz for Rayleigh waves. The fundamental ellipticity peak frequency is around 8 Hz.
Different inversion targets were used. Good models were obtained by a joint inversion of Love and Rayleigh wave dispersion curves without ellipticity information and including the Rayleigh wave ellipticity angle corresponding to a retrograde particle motion. The structure can be explained by models with a main impedance contrast at 8 m depth (inversion without ellipticity target) or by a more gradual increase of the shear-wave velocity (inversions including the ellipticity curve). The V_{S30} of the best models for the first inversion target is about 547 m/s, corresponding to soil class E in both EC8 and SIA261. For the other inversion target, V_{S30} is about 470 m/s, corresponding to soil class B in EC8 and E in SIA261. For the ensemble of models from both inversion targets, V_{S30} is about 509 m/s, corresponding to class E in SIA261 and between soil class B and E for EC8.

Acknowledgements

The authors thank Marthe Faber and David Farsky for their help during the array measurements.

References

Aki, K. (1957). Space and time spectra of stationary stochastic waves, with special reference to microtremors. *Bull. Earthquake Res. Inst. Tokyo Univ.*, 35:415–456.

Bettig, B., Bard, P.-Y., Scherbaum, F., Riepl, J., Cotton, F., Cornou, C., and Hatzfeld, D. (2001). Analysis of dense array noise measurements using the modified spatial auto-correlation method (SPAC): application to the Grenoble area. *Boll. Geof. Teor. Appl.*, 42:281–304.

Burjánek, J., Gassner-Stamm, G., Poggi, V., Moore, J. R., and Fäh, D. (2010). Ambient vibration analysis of an unstable mountain slope. *Geophys. J. Int.*, 180:820–828.

Burjánek, J., Moore, J. R., Molina, F. X. Y., and Fäh, D. (2012). Instrumental evidence of normal mode rock slope vibration. *Geophys. J. Int.*, 188:559–569.

Fäh, D., Wathelet, M., Kristekova, M., Havenith, H., Endrun, B., Stamm, G., Poggi, V., Burjanek, J., and Cornou, C. (2009). Using ellipticity information for site characterisation. NERIES deliverable JRA4 D4, available at http://www.neries-eu.org.

Hobiger, M., Bard, P.-Y., Cornou, C., and Le Bihan, N. (2009). Single station determination of Rayleigh wave ellipticity by using the random decrement technique (RayDec). *Geophys. Res. Lett.*, 36.

Joyner, W. B., Warrick, R. E., and Fumal, T. E. (1981). The effect of Quaternary alluvium on strong ground motion in the Coyote Lake, California, earthquake of 1979. *Bull. Seismol. Soc. Am.*, 71(4):1333–1349.

Maranò, S., Hobiger, M., Bergamo, P., and Fäh, D. (2017). Analysis of rayleigh waves with circular wavefront: a maximum likelihood approach. *Geophys. J. Int.*, 210:1570–1580.

Maranò, S., Reller, C., Loeliger, H.-A., and Fäh, D. (2012). Seismic waves estimation and wavefield decomposition: Application to ambient vibrations. *Geophys. J. Int.*, 191:175–188.

Poggi, V., Edwards, B., and Fäh, D. (2012). Characterizing the Vertical-to-Horizontal ratio of ground motion at soft-sediment sites. *Bull. Seismol. Soc. Am.*, 102(6):2741–2756.

Poggi, V. and Fäh, D. (2010). Estimating Rayleigh wave particle motion from three-component array analysis of ambient vibrations. *Geophys. J. Int.*, 180:251–267.